JOURNAL OF PETROLOGY | VOLUME 48 | NUMBER 5 | PAGES 853–883 | 2007 | doi:10.1093/petrology/egm004

# Evolution of Mafic Alkaline Melts Crystallized in the Uppermost Lithospheric Mantle: a Melt Inclusion Study of Olivine-Clinopyroxenite Xenoliths, Northern Hungary

**ZOLTÁN ZAJACZ[1]*, ISTVÁN KOVÁCS[2], CSABA SZABÓ[3], WERNER HALTER[1] AND THOMAS PETTKE[4]**

[1]DEPARTMENT OF EARTH SCIENCES, INSTITUTE OF ISOTOPE GEOCHEMISTRY AND MINERAL RESOURCES, ETH ZÜRICH, 8092 ZÜRICH, SWITZERLAND

[2]RESEARCH SCHOOL OF EARTH SCIENCES, BUILDING 61 MILLS ROAD, THE AUSTRALIAN NATIONAL UNIVERSITY, CANBERRA, ACT 0200, AUSTRALIA

[3]LITHOSPHERE FLUID RESEARCH LABORATORY, INSTITUTE OF GEOGRAPHY AND EARTH SCIENCES, EÖTVÖS UNIVERSITY BUDAPEST (ELTE), PAZMANY SETANY 1/c, BUDAPEST, HUNGARY, H-1117

[4]UNIVERSITY OF BERN, INSTITUTE OF GEOLOGICAL SCIENCES, BALTZERSTRASSE 1–3, CH-3012 BERN, SWITZERLAND

**RECEIVED APRIL 7, 2006; ACCEPTED FEBRUARY 2, 2007**
**ADVANCE ACCESS PUBLICATION APRIL 16, 2007**

*Olivine-clinopyroxenite xenoliths exhumed in alkali basalts (sensu lato) in the Nógrád–Gömör Volcanic Field (NGVF), northern Hungary, contain abundant silicate melt inclusions. Geothermobarometric calculations indicate that these xenoliths crystallized as cumulates in the upper mantle near the Moho. These cumulate xenoliths are considered to represent a period of Moho underplating by mafic alkaline magmas prior to the onset of Late Tertiary alkaline volcanism in the Carpathian–Pannonian region. The major and trace element compositions of silicate melt inclusions in olivine display an evolutionary trend characterized by a strong decrease in $CaO/Al_2O_3$. The parental melt of the cumulates was a basanite formed by low-degree (~2%) partial melting of a garnet peridotite source. The compositional trend of the silicate melt inclusions, textural features, and modelling with pMELTS show that the parental melt evolved by major clinopyroxene and minor olivine crystallization followed by the appearance of amphibole simultaneously with significant resorption of the earlier clinopyroxene and olivine. The resulting residual melt was highly enriched in $Al_2O_3$, alkalis and most incompatible trace elements. This type of melt is likely to infiltrate and react with surrounding mantle peridotite as a metasomatic agent. It might also form high-pressure pegmatite-like bodies in the mantle that might be the source of the amphibole and sanidine megacrysts also found in the alkali basalts of the NGVF. Preferential remelting of the later-formed (i.e. lower temperature) mineral assemblage (amphibole, sanidine, residual glass) might have significantly contaminated the host alkaline mafic lavas, increasing their $Al_2O_3$ and total alkali contents and, therefore, reducing their MgO, FeO and CaO content.*

KEY WORDS: *silicate melt inclusions; geochemistry; petrogenesis; Nógrád–Gömör Volcanic Field; Pannonian Basin*

## INTRODUCTION

Olivine-clinopyroxenite and clinopyroxenite xenoliths, and clinopyroxene and amphibole megacrysts are common within the alkali basalts in the Pannonian Basin (Embey-Isztin *et al.*, 1990, 1993; Downes *et al.*, 1995; Dobosi & Jenner, 1999; Dobosi *et al.*, 2003; Török *et al.*, 2003; Kovács *et al.*, 2004) and worldwide (Frey & Prinz, 1978; Irving & Frey, 1984; Wilson & Downes, 1991; Shaw

*Corresponding author. Telephone: +41-44-6320734. Fax: +41-44-6321827. E-mail: zajacz@erdw.ethz.ch

& Eyzaguirre, 2000; Chen *et al.*, 2001; Bondi *et al.*, 2002; Riley & Bailey, 2003; Liu *et al.*, 2005). In most studies they have been interpreted as high-pressure crystallization products of melts similar in composition to the host alkaline basalts, based on thermobarometric calculations, isotopic ratios and estimated equilibrium melt compositions (Irving, 1974; Stuckless & Irving, 1976; Frey & Prinz, 1978; Shaw & Eyzaguirre, 2000; Chen *et al.*, 2001; Bondi *et al.*, 2002; Dobosi *et al.*, 2003; Riley & Bailey, 2003; Downes *et al.*, 2004; Kovács *et al.*, 2004; Shaw *et al.*, 2005). Alternatively, the olivine-clinopyroxenite xenoliths have been interpreted as the products of metamorphic segregation during anatexis of the surrounding mantle region (Chen *et al.*, 2001). Alkali feldspar phenocrysts have also been reported in a number of alkali basalts (Frey & Prinz, 1978; Aspen *et al.*, 1990; Riley & Bailey, 2003), but the origin of the siliceous melt from which they crystallized has not yet been identified. Only Irving (1974) suggested that they might form as near-solidus crystallization products of primitive alkaline melts in the mantle.

In the case of crystallization of basaltic melts, separation of the mafic minerals forms cumulus ultramafic rocks composed of clinopyroxene, olivine and usually Al-spinel; such rocks are not representative of the parental melt, thus mineral–melt equilibria are needed to constrain the geochemical character of the parental melt.

Here we study silicate melt inclusions (SMIs) from olivine-clinopyroxenite xenoliths hosted in alkali basalts of the Nógrád–Gömör Volcanic Field (NGVF), northern Pannonian Basin (Hungary), to directly obtain the composition of the parental melt of the xenoliths. Most previous studies of SMIs have focused on melt inclusions in phenocrysts in volcanic rocks (e.g. Nielsen *et al.*, 1995; Kamenetsky & Clocchiatti, 1996; Kamenetsky *et al.*, 1997; Xu *et al.*, 1999; Norman *et al.*, 2002; Bertagnini *et al.*, 2003; Cervantes & Wallace, 2003; Danyushevsky *et al.*, 2003; Maclennan *et al.*, 2003; Schiano, 2003; Schiano *et al.*, 2004). Here we present data on SMIs within the constituent minerals of cumulate xenoliths derived by fragmentation of a magma body that crystallized slowly near the Moho.

The major goals of this paper are fourfold: (1) to provide additional information on the genesis of Type-II (mostly clinopyroxenite and olivine-clinopyroxenite) xenoliths; (2) to obtain a better understanding of the evolution of alkali basaltic systems; (3) to test of the representative nature of olivine-hosted melt inclusions in these xenoliths; (4) to provide new information on the evolution of the Carpathian–Pannonian region. We reproduced the original composition and the chemical evolution of the parental melt based on electron microprobe analyses (EPMA) of homogenized melt inclusions and laser ablation inductively coupled plasma mass spectrometry (LA-ICPMS) analysis of unheated multiphase inclusions in olivine. Petrogenetic models, based on the major and trace element composition of the SMIs and the rock-forming minerals, are presented and used to constrain the formation and evolution of the parental melt.

## GEOLOGICAL SETTING

The Nógrád–Gömör Volcanic Field (NGVF) at the northern margin of the Pannonian Basin (Northern Hungary–Southern Slovakia) (Fig. 1) is mostly composed of Plio-Pleistocene alkali basalts (*sensu lato*). It is surrounded by the Miocene, subduction-related, Inner Carpathian calc-alkaline volcanic belt. The Pannonian Basin was formed as a result of lithospheric stretching in two major extensional episodes: (1) an Early to Middle Miocene passive rifting phase driven by subduction rollback (Royden *et al.*, 1983*a*, 1983*b*; Csontos, 1995; Fodor *et al.*, 1999); (2) a Late Miocene syn- to post-rift phase accompanied by asthenospheric upwelling and thinning of the mantle lithosphere (Royden *et al.*, 1983*a*, 1983*b*; Huismans *et al.*, 2001). The alkali basalts were erupted in the post-extensional phase and sampled the lithospheric section beneath the region, transporting a large quantity of peridotite (Type-I), ultramafic cumulate (Type-II) and crustal xenoliths to the surface (Embey-Isztin *et al.*, 1993; Szabó & Taylor, 1994; Embey-Isztin & Dobosi, 1995; Zajacz & Szabó, 2003; Kovács *et al.*, 2004; Seghedi *et al.*, 2004) (Fig. 1). The xenoliths investigated in this study were collected from the Nagy-Salgó volcano. The locality is a well-preserved basanite volcanic neck containing a high abundance of olivine-clinopyroxenite and wehrlite xenoliths. The host rock is Pliocene (5·27 Ma) in age (Szabó *et al.*, unpublished data).

## PETROGRAPHY OF THE CUMULATE XENOLITHS AND SILICATE MELT INCLUSIONS

In the NGVF several eruptive centres contain clinopyroxene- and olivine-rich xenoliths. In some locations amphibole is also typical and has been interpreted as a metasomatic alteration product of the clinopyroxene (Kovács *et al.*, 2004). The xenoliths selected for a detailed melt inclusion study are mostly olivine-clinopyroxenites, and subordinately wehrlites. Regardless of variations in the clinopyroxene to olivine ratio, the xenoliths are texturally similar. The volume proportion of olivine ranges from 20% to 40% (Table 1). Both the clinopyroxene and the olivine are euhedral or subhedral and their grain sizes are between 0·5 and 5 mm (Fig. 2a). The edges of the olivine crystals are resorbed, whereas the clinopyroxenes typically display a narrow reaction rim (Fig. 2b and c). In addition to the major rock-forming clinopyroxene and olivine, two types of interstitial phase assemblages are present: (1) a

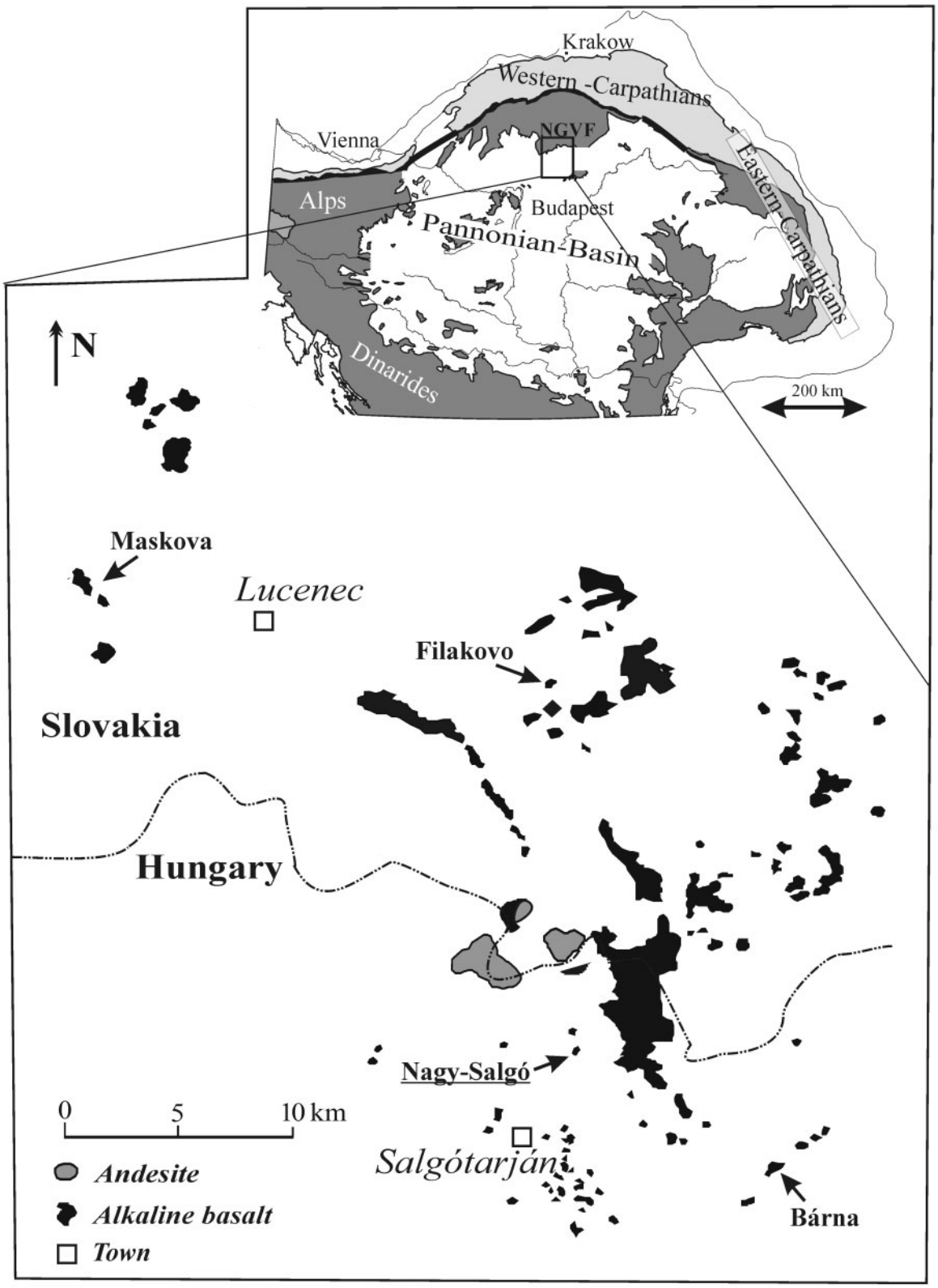


**Fig. 1.** Map of the Nógrád–Gömör Volcanic Field. The most important alkaline basalt (*sensu lato*) occurrences are shown; the studied xenoliths were collected from Nagy-Salgó.

light-coloured assemblage composed of euhedral alkali feldspar, clinopyroxene, Ti-magnetite, apatite and residual glass (Fig. 2d and e); (2) a dark-coloured assemblage of partially decomposed amphibole displaying evidence of breakdown to rhönite, nepheline, clinopyroxene, olivine and Ti-magnetite. In some xenoliths the amphibole is completely decomposed and only the residual minerals are present (Fig. 2f). Interstitial phase assemblage (1) is typical of all the xenoliths whereas interstitial phase assemblage (2) is observed in small quantities only in a few xenoliths (Table 1). Despite the uniform texture and mineralogy there is a significant variation in the melt and fluid inclusion content of the xenoliths. Out of five large (3–5 cm in diameter) unaltered xenoliths selected for investigation, only two contained SMIs in olivine large enough for analysis (>10 μm), whereas clinopyroxenes are generally rich in SMIs and $CO_2$ inclusions (Table 1). As the main focus of our study is on olivine-hosted SMIs, these two xenoliths (NNS07 and NNS08) have been selected for detailed analytical work.

Olivines contain SMIs either as single inclusions or in clusters. They are generally absent from the cores of large olivine crystals. The inclusions are always rounded and almost isometric (Fig. 3a–c), ranging from 8 to 40 μm in diameter. They occur as partially recrystallized multiphase assemblages of clinopyroxene (20–30 vol. %), Al-spinel (1–3 vol. %), rhönite (10–20 vol. %) and/or Ti-rich pargasitic amphibole (5–15 vol. %), together with residual glass (40–60 vol. %) and a $CO_2$ bubble (4–8 vol. %). Small sulphide blebs are also present in several inclusions (Fig. 3c).

Clinopyroxene crystals are packed with elongated and oriented SMIs. Their size ranges from submicroscopic to 30 μm in diameter (Fig. 3d). They are usually present from grain cores to rims. SMI size distribution sometimes shows periodic zonation with alternating zones of small (submicroscopic to 5 μm in diameter) and large inclusions (from 5 μm to 30 μm in diameter) following the growth direction of the clinopyroxene. They are partially recrystallized and composed of clinopyroxene (0–20 vol. %), Ti-rich pargasite (0–10 vol. %), Al-spinel (1–3 vol. %), Ti-magnetite (0–2 vol. %), residual glass (65–95 vol. %) and a $CO_2$ bubble. The $CO_2$ fluid to melt ratio is variable, suggesting accidental entrapment of a previously exsolved fluid phase along with the melt (heterogeneous entrapment) (Fig. 3d). Individual $CO_2$ inclusions have also been identified in clinopyroxene. Most of the $CO_2$ inclusions have leaked; however, some smaller ones (generally <8 μm) preserve two phases or liquid $CO_2$ at room temperature. The presence of $CO_2$ was determined by Raman spectroscopy; significant $H_2O$ was not detected in the fluid phase.

The compositions of the daughter phases in the SMIs in both olivine and clinopyroxene are given in Table 2.

## ANALYTICAL TECHNIQUES

SMIs were reheated using a Linkam TS1500 stage at the Lithosphere Fluid Research Laboratory, Eötvös University, Budapest. Heating was carried out in a nitrogen atmosphere on separated and doubly polished olivine grains. The initial high (30°C/min) heating rate was

*Table 1: Modal composition (vol. %) and inclusion content of the studied xenoliths*

| Xenolith: Rock type: | NNS07 wehrlite | NNS08 olivine-clinopyroxenite | NNS09 olivine-clinopyroxenite | NNS10 olivine-clinopyroxenite | NNS11 olivine-clinopyroxenite |
|---|---|---|---|---|---|
| Clinopyroxene | 53 | 54 | 63 | 76 | 68 |
| Olivine | 42 | 33 | 31 | 20 | 24 |
| Amphibole* | 0 | 11 | 4 | 0 | 3 |
| Intercumulus phase assemblage | 5 | 2 | 2 | 4 | 5 |
| Inclusions in olivine | abundant primary SMIs and a few sulphide inclusions | primary SMIs in low abundance | small (<10 μm) pseudosecondary SMIs | sulphide inclusions in low abundance | small (<10 μm) pseudosecondary SMIs |
| Inclusions in clinopyroxene | abundant primary SMIs and $CO_2$ fluid inclusions and a few sulphide inclusions | abundant primary SMIs and $CO_2$ fluid inclusions | abundant primary SMIs and $CO_2$ fluid inclusions | abundant primary SMIs and $CO_2$ fluid inclusions | abundant, but very small (mostly <1 μm) SMIs |

*Including breakdown products of amphibole.

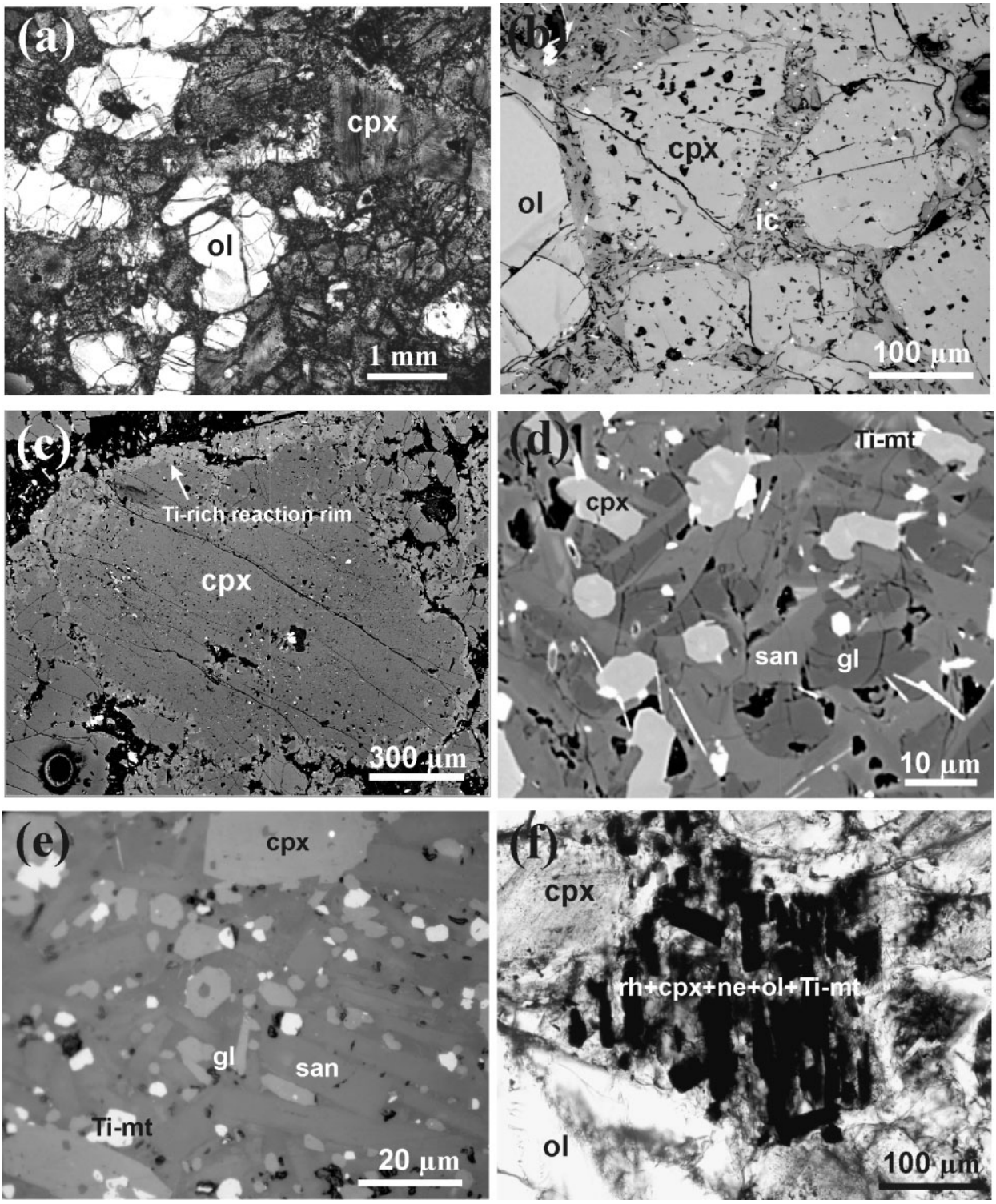


**Fig. 2.** Petrography of the xenoliths. (a) Texture of a typical olivine-clinopyroxenite xenolith (NNS08); (b) mode of occurrence of the intercumulus phase (NNS07); (c) BSE image of a typical clinopyroxene crystal in the cumulate with Ti-rich late-stage rim (NNS08); (d) BSE image of the intercumulus phase (NNS07); (e) image of the intercumulus phase in reflected light (NNS07); (f) breakdown assemblage after amphibole in transmitted light (NNS08). cpx, clinopyroxene; ol, olivine; ic, intercumulus phase; san, sanidine; gl, glass; Ti-mt, Ti-magnetite; rh, rhönite; ne, nepheline.

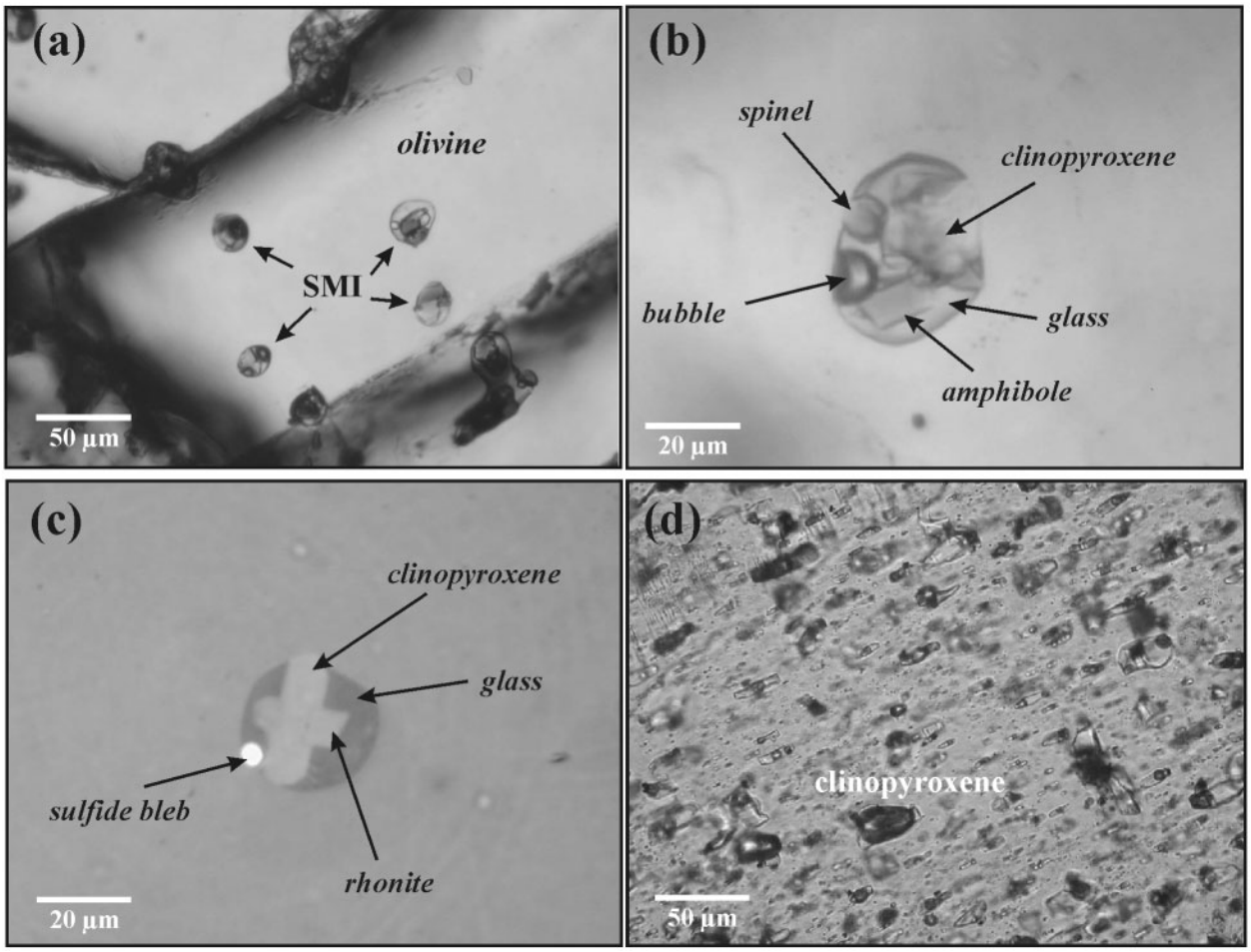


**Fig. 3.** Petrography of the melt inclusions. (a) Multiphase SMIs in olivine (NNS07); (b) close-up of a non-exposed multiphase melt inclusion in olivine (NNS07); (c) melt inclusion containing sulphide bleb in olivine (RL) (NNS07); (d) clinopyroxene crystal packed with elongated and oriented melt inclusions and dark $CO_2$ fluid inclusions (NNS07).

progressively decreased to 5°C/min approaching the melting temperature of the daughter phases. The stage allowed a cooling rate of ~300°C/min in the high-temperature range (above the glass transition temperature).

Homogenized SMIs and the daughter phases of the SMIs were analyzed at the University of Vienna on a Cameca SX-100 electron microprobe using a 15 kV acceleration voltage, 20 nA beam current, 20 s peak and 10 s background count time for each element. On all heated SMIs, at least two analyses were carried out to test their homogeneity. Compositions of the rock-forming minerals and interstitial phase assemblages were determined at ETH Zürich using a JEOL SUPERPROBE JXA-8200 electron microprobe. A 15 kV acceleration voltage and 15 nA beam current were used and a 20 s counting time was applied for each element. For mineral analysis a 2 µm beam diameter was used; for glasses, the beam diameter was enlarged (to 5 or 10 µm) and the beam current was reduced to 10 nA. The following standards were used: wollastonite for $SiO_2$ and CaO; forsterite for MgO; aegirine for $Na_2O$; sanidine for $K_2O$; apatite for $P_2O_5$; natural oxides for FeO, $TiO_2$ and MnO.

LA-ICPMS analysis of the SMIs and their host clinopyroxene and olivine was carried out at ETH Zürich, using an ArF excimer UV (193 nm) laser source at 70mJ output energy and a repetition rate of 10 Hz. The beam diameter varied between 20 and 60 µm for SMI measurements, whereas for bulk measurement of the interstitial phase assemblages a beam diameter of 110 µm was used. SMIs were analyzed and the data reduction was performed using the method of Halter *et al.* (2002) (see Appendix for further details). Only unexposed SMIs were measured. A beam diameter slightly larger than the actual size of the inclusion was used to avoid incomplete sampling of the heterogeneous SMIs. Melt inclusions deeper than 30 µm beneath the section surface were not measured. Inclusion signals shorter than 15 readings were not considered. In the case of SMI measurements, a 10 ms dwell time was used for all elements.

However, for the clinopyroxene host measurements we used an extended (20 ms) dwell time for Yb and Lu because of their low concentrations. Quantification of the interstitial phases was based on analysis of all the major elements and normalization to 100% without application of any internal standard (Halter *et al.*, 2002). For external standardization the NBS SRM 610 glass standard was used.

Uncertainties are variable for each single analysis, but for SMIs are mainly in the range 5–20 relative % for concentrations of large ion lithophile elements (LILE), high field strength elements (HFSE) and light rare earth elements (LREE), and 15–50 relative % for heavy REE (HREE), which are present in very low concentrations. In the case of clinopyroxene, amphibole, and bulk intercumulus phase analyses uncertainties are below 15 relative% for most elements.

## COMPOSITIONS OF THE ROCK-FORMING MINERAL PHASES

### Major mineral constituents

The clinopyroxene is diopsidic and displays almost homogeneous cores surrounded by reaction rims (Fig. 2c). The compositional transition between the cores and the rims is not continuous and it shows clustering of mg-numbers around 82–85 (core) and 78–80 (rim), respectively

*Table 2: Average composition of the daughter minerals and the residual glass in olivine- and clinopyroxene-hosted silicate melt inclusions in xenolith NNS07 (in wt %)*

| Daughter mineral: | clinopyroxene | | | amphibole | | rhönite | | |
|---|---|---|---|---|---|---|---|---|
| Host of SMI: | olivine (4)* | σ | cpx (1) | cpx (2) | σ | olivine (5) | σ | cpx (1) |
| $SiO_2$ | 43·7 | 1·7 | 48·8 | 43·3 | 2·3 | 25·7 | 0·7 | 27·0 |
| $TiO_2$ | 4·63 | 1·01 | 1·07 | 4·55 | 0·35 | 10·53 | 1·37 | 6·51 |
| $Al_2O_3$ | 11·29 | 1·60 | 6·85 | 13·39 | 1·07 | 17·93 | 0·07 | 17·73 |
| $Cr_2O_3$ | 0·21 | 0·19 | 0·12 | 0·03 | 0·01 | 0·25 | 1·16 | 0·29 |
| FeO | 6·45 | 1·22 | 6·91 | 10·76 | 0·26 | 20·0 | 1·4 | 21·1 |
| MnO | 0·12 | 0·09 | 0·16 | 0·16 | 0·06 | 0·12 | 0·05 | 0·18 |
| MgO | 11·09 | 1·12 | 14·31 | 13·31 | 0·88 | 13·33 | 0·30 | 13·93 |
| CaO | 21·67 | 0·54 | 21·07 | 10·05 | 0·94 | 10·80 | 0·63 | 11·03 |
| $Na_2O$ | 1·03 | 0·29 | 0·56 | 3·08 | 0·31 | 1·62 | 0·31 | 2·10 |
| $K_2O$ | 0·10 | 0·07 | 0·01 | 0·67 | 0·14 | 0·01 | 0·01 | 0·00 |
| Total | 100·30 | | 99·85 | 99·27 | | 100·35 | | 99·79 |

| Daughter mineral: | Al-spinel | | | Ti-magnetite | | residual glass | | | |
|---|---|---|---|---|---|---|---|---|---|
| Host of SMI: | olivine (1) | cpx (2) | σ | cpx (2) | σ | olivine (5) | σ | cpx (4) | σ |
| $SiO_2$ | 0·08 | 0·29 | 0·12 | 0·68 | 0·75 | 57·1 | 2·8 | 66·7 | 1·39 |
| $TiO_2$ | 0·49 | 0·97 | 0·01 | 9·04 | 0·41 | 0·21 | 0·10 | 0·15 | 0·05 |
| $Al_2O_3$ | 63·5 | 47·0 | 0·50 | 9·43 | 4·82 | 29·1 | 1·7 | 21·7 | 0·53 |
| $Cr_2O_3$ | 0·79 | 4·66 | 1·75 | 2·34 | 0·91 | n.a. | | n.a. | |
| FeO | 18·4 | 34·6 | 2·94 | 74·4 | 6·4 | 0·99 | 0·13 | 0·42 | 0·11 |
| MnO | 0·12 | 0·22 | 0·01 | 0·48 | 0·18 | n.a. | | n.a. | |
| MgO | 17·48 | 10·68 | 2·98 | 2·02 | 0·79 | 0·30 | 0·24 | 0·20 | 0·38 |
| CaO | 0·05 | 0·38 | 0·05 | 0·77 | 0·44 | 0·28 | 0·20 | 0·67 | 0·25 |
| $Na_2O$ | n.a. | n.a. | | n.a. | | 9·47 | 0·64 | 4·75 | 3·00 |
| $K_2O$ | n.a. | n.a. | | n.a. | | 3·06 | 0·40 | 3·28 | 1·61 |
| Total | 100·88 | 98·84 | | 99·17 | | 100·50 | | 97·88 | |

*Number of analyses.
n.a., not analyzed.

(Table 2). Both the jadeite component and $TiO_2$ content increase from core to rim (Table 3). The reaction rim of the clinopyroxene can be distinguished on back-scattered electron (BSE) images (Fig. 2c).

Trace element concentrations (Table 4) show no obvious trends as a function of mg-number; however, rim measurements display the lowest mg-number and the highest incompatible trace element concentrations. It should be

*Table 3: Composition of selected xenolith-forming clinopyroxenes (in wt %) and results of geothermobarometry calculations using the method of Putirka* et al. *(2003)*

| Xenolith: | NNS07 | | | | | NNS08 | | | | | |
|---|---|---|---|---|---|---|---|---|---|---|---|
| Grain: | 1 | 1 | 2 | 2 | 3 | 1 | 1 | 2 | 2 | 3 | 3 |
| Location: | core | ovg | core | ovg | core | core | ovg | core | ovg | core | ovg |
| $SiO_2$ | 49·0 | 46·0 | 48·9 | 47·2 | 48·8 | 48·7 | 44·5 | 49·5 | 47·2 | 51·8 | 48·1 |
| $TiO_2$ | 1·25 | 3·92 | 1·41 | 2·93 | 1·18 | 1·48 | 4·81 | 0·91 | 1·77 | 0·62 | 2·01 |
| $Al_2O_3$ | 6·06 | 7·02 | 5·97 | 6·29 | 6·26 | 6·94 | 9·20 | 5·41 | 7·96 | 4·11 | 5·58 |
| $Cr_2O_3$ | 0·31 | 0·17 | 0·21 | 0·24 | 0·30 | 0·24 | 0·19 | 0·26 | 0·19 | 0·16 | 0·39 |
| FeO | 5·14 | 6·18 | 5·13 | 5·88 | 5·74 | 5·01 | 5·18 | 5·42 | 5·91 | 5·19 | 6·03 |
| MnO | 0·07 | 0·05 | 0·08 | 0·05 | 0·09 | 0·07 | 0·05 | 0·10 | 0·09 | 0·12 | 0·05 |
| MgO | 14·9 | 12·8 | 15·1 | 13·4 | 15·0 | 14·5 | 12·4 | 14·7 | 13·3 | 15·4 | 13·7 |
| CaO | 22·6 | 22·9 | 22·4 | 23·1 | 21·9 | 22·4 | 22·9 | 22·4 | 22·2 | 22·7 | 23·2 |
| $Na_2O$ | 0·59 | 0·82 | 0·51 | 0·73 | 0·55 | 0·58 | 0·84 | 0·47 | 0·69 | 0·44 | 0·69 |
| $K_2O$ | 0·03 | 0·03 | 0·02 | 0·01 | 0·02 | 0·01 | 0·04 | 0·01 | 0·02 | 0·01 | 0·01 |
| $P_2O_5$ | 0·01 | 0·03 | 0·00 | 0·01 | 0·01 | 0·01 | 0·02 | 0·01 | 0·00 | 0·01 | 0·01 |
| Total | 99·95 | 99·89 | 99·83 | 99·84 | 99·86 | 100·03 | 100·18 | 99·17 | 99·36 | 100·57 | 99·85 |
| mg-no. | 83·8 | 78·7 | 84·0 | 80·2 | 82·3 | 83·8 | 81·0 | 82·8 | 80·0 | 84·1 | 80·2 |
| *P* (kbar) | 11·6 | 8·7 | 10·9 | 9·9 | 11·3 | 11·6 | 12 | 10·3 | 11·1 | 9·8 | 9·9 |
| *T* (°C) | 1197 | 1123 | 1192 | 1130 | 1198 | 1199 | 1152 | 1186 | 1145 | 1179 | 1129 |
| *Cations per 6 oxygens* | | | | | | | | | | | |
| Si | 1·81 | 1·72 | 1·81 | 1·76 | 1·81 | 1·80 | 1·66 | 1·84 | 1·76 | 1·89 | 1·80 |
| Al(IV) | 0·189 | 0·277 | 0·190 | 0·235 | 0·192 | 0·203 | 0·341 | 0·158 | 0·237 | 0·108 | 0·203 |
| Al(VI) | 0·075 | 0·033 | 0·070 | 0·042 | 0·081 | 0·098 | 0·063 | 0·080 | 0·113 | 0·069 | 0·043 |
| $Fe^{3+}$ | 0·077 | 0·077 | 0·072 | 0·075 | 0·075 | 0·058 | 0·063 | 0·053 | 0·069 | 0·030 | 0·086 |
| $Fe^{2+}$ | 0·082 | 0·116 | 0·086 | 0·108 | 0·102 | 0·097 | 0·098 | 0·115 | 0·115 | 0·128 | 0·102 |
| Mg | 0·821 | 0·715 | 0·834 | 0·744 | 0·826 | 0·797 | 0·690 | 0·815 | 0·741 | 0·840 | 0·763 |
| Mn | 0·002 | 0·002 | 0·002 | 0·002 | 0·003 | 0·002 | 0·002 | 0·003 | 0·003 | 0·004 | 0·002 |
| Ti | 0·035 | 0·110 | 0·039 | 0·082 | 0·033 | 0·041 | 0·135 | 0·025 | 0·050 | 0·017 | 0·056 |
| Ca | 0·895 | 0·919 | 0·888 | 0·925 | 0·869 | 0·887 | 0·914 | 0·893 | 0·888 | 0·890 | 0·929 |
| K | 0·000 | 0·001 | 0·001 | 0·001 | 0·001 | 0·001 | 0·002 | 0·001 | 0·001 | 0·000 | 0·001 |
| Na | 0·042 | 0·060 | 0·037 | 0·053 | 0·039 | 0·041 | 0·061 | 0·034 | 0·050 | 0·031 | 0·050 |
| Cr | 0·009 | 0·005 | 0·006 | 0·007 | 0·009 | 0·007 | 0·005 | 0·008 | 0·005 | 0·005 | 0·012 |
| *End-members (mol%)** | | | | | | | | | | | |
| DiHd | 0·775 | 0·776 | 0·770 | 0·800 | 0·744 | 0·750 | 0·737 | 0·783 | 0·732 | 0·812 | 0·816 |
| EnFs | 0·064 | 0·028 | 0·075 | 0·026 | 0·092 | 0·072 | 0·025 | 0·074 | 0·062 | 0·078 | 0·024 |
| CaTs | 0·033 | 0·000 | 0·033 | 0·000 | 0·042 | 0·057 | 0·002 | 0·046 | 0·063 | 0·039 | 0·000 |
| Jd | 0·042 | 0·033 | 0·037 | 0·042 | 0·039 | 0·041 | 0·061 | 0·034 | 0·050 | 0·031 | 0·043 |
| CaTi | 0·078 | 0·138 | 0·078 | 0·118 | 0·075 | 0·073 | 0·169 | 0·056 | 0·087 | 0·034 | 0·101 |
| CrCaTs | 0·009 | 0·005 | 0·006 | 0·007 | 0·009 | 0·007 | 0·005 | 0·008 | 0·005 | 0·005 | 0·012 |

ovg, overgrowth.
*End-members are calculated with the method of Putrika (1999). DiHd, diopside + hedenbergite; EnFs, enstatite + ferrosilite; CaTs, Ca-Tschermak; Jd, jadeite; CaTi, $CaTi_2AlO_6$; CrCaTs, $CaCr_2SiO_6$.

*Table 4: Trace element composition of the clinopyroxenes (in ppm)*

| Xenolith: | NNS07 | | | | | | | | | | | |
|---|---|---|---|---|---|---|---|---|---|---|---|---|
| Grain: | 1 | 1 | 1 | 1 | 1 | 1 | 2 | 2 | 2 | 2 | 3 | 3 |
| Sc | 57 | 60 | 52 | 58 | 56 | 59 | 52 | 59 | 50 | 52 | 60 | 56 |
| V | 307 | 400 | 306 | 321 | 281 | 280 | 273 | 289 | 212 | 154 | 280 | 288 |
| Cr | 1355 | 2437 | 1487 | 841 | 2912 | 3733 | 4202 | 3091 | 1796 | 651 | 2703 | 2211 |
| Ni | 205 | 211 | 137 | 183 | 169 | 126 | 206 | 190 | 162 | 126 | 123 | 136 |
| Cu | 13·90 | <3·74 | 6·28 | 9·71 | <3·26 | 4·52 | 5·96 | <2·09 | 2·21 | 6·41 | 17·60 | 3·30 |
| Rb* | <0·48 | <0·43 | <0·36 | 0·36 | <0·28 | <0·10 | <0·53 | <0·34 | <0·23 | <0·08 | <0·10 | <0·12 |
| Sr | 34 | 40 | 31 | 37 | 37 | 41 | 39 | 44 | 42 | 59 | 38 | 42 |
| Y | 12·8 | 12·7 | 11·1 | 13·3 | 11·4 | 11·5 | 10·2 | 11·8 | 9·2 | 11·3 | 12·6 | 11·5 |
| Zr | 30 | 18 | 29 | 36 | 30 | 33 | 25 | 45 | 35 | 50 | 32 | 44 |
| Nb | 0·22 | <0·24 | <0·26 | 0·29 | <0·28 | 0·16 | <0·29 | 0·21 | <0·14 | <0·06 | 0·12 | 0·49 |
| Ba | 1·61 | 1·24 | <0·73 | 1·29 | <0·61 | <0·18 | <1·67 | <1·23 | <0·49 | <0·33 | <0·22 | 1·31 |
| La | 1·40 | 0·78 | 1·81 | 2·51 | 2·01 | 1·85 | 2·22 | 4·62 | 3·24 | 4·82 | 2·55 | 2·85 |
| Ce | 5·7 | 3·6 | 5·4 | 6·2 | 5·7 | 6·1 | 6·7 | 11·1 | 8·7 | 11·9 | 7·0 | 7·5 |
| Nd | 5·1 | 7·9 | 6·5 | 5·6 | 5·8 | 6·6 | 5·4 | 8·0 | 7·0 | 8·1 | 6·9 | 6·7 |
| Sm | 2·19 | 3·44 | 1·99 | 2·91 | 2·65 | 2·02 | 1·99 | 2·94 | 1·49 | 2·56 | 2·21 | 3·77 |
| Eu | 0·52 | 1·32 | 0·43 | 0·92 | 0·95 | 0·89 | 0·62 | 1·27 | 0·86 | 1·01 | 0·91 | 0·81 |
| Gd | 1·34 | 2·44 | 3·14 | 1·77 | 3·75 | 2·48 | 2·43 | 3·78 | 1·89 | 2·48 | 2·11 | 3·15 |
| Yb | 1·21 | 1·58 | <0·68 | 1·05 | 0·95 | 0·94 | 1·60 | 1·30 | 0·63 | 1·11 | 0·77 | 0·76 |
| Lu | <0·10 | 0·15 | 0·18 | 0·18 | 0·10 | 0·12 | <0·12 | 0·20 | <0·08 | 0·14 | 0·15 | 0·07 |
| Hf | 1·58 | 1·11 | 0·85 | 1·34 | 1·21 | 1·06 | 0·60 | 1·72 | 1·65 | 1·64 | 1·29 | 1·25 |
| Th | 0·15 | <0·13 | 0·33 | 0·16 | 0·25 | 0·17 | 0·16 | <0·11 | 0·12 | 0·18 | 0·36 | 0·34 |
| U | <0·13 | <0·12 | <0·11 | <0·19 | <0·09 | 0·09 | <0·15 | <0·11 | <0·07 | <0·05 | 0·11 | 0·18 |
| Pr | 1·14 | 0·97 | 0·96 | 1·37 | 1·38 | 1·10 | 1·21 | 1·44 | 1·15 | 1·56 | 1·07 | 1·21 |
| Er | 1·56 | 2·68 | 0·75 | 1·97 | 0·71 | 1·39 | 1·03 | 1·73 | 0·77 | 1·19 | 1·23 | 1·68 |
| Ho | 0·53 | 0·59 | 0·48 | 0·79 | 0·37 | 0·47 | 0·51 | 0·42 | 0·33 | 0·43 | 0·61 | 0·60 |
| Tb | 0·56 | 0·40 | 0·59 | 0·32 | 0·48 | 0·45 | 0·42 | 0·34 | 0·46 | 0·42 | 0·44 | 0·33 |
| Dy | 2·12 | 3·67 | 2·22 | 3·16 | 2·68 | 2·62 | 1·93 | 3·14 | 1·93 | 1·83 | 3·13 | 2·61 |
| Tm | <0·11 | <0·18 | 0·27 | <0·10 | 0·28 | 0·20 | <0·12 | <0·09 | 0·12 | 0·15 | 0·19 | 0·16 |

| Xenolith: | NNS08 | | | | | | | | | | | |
|---|---|---|---|---|---|---|---|---|---|---|---|---|
| Grain: | 1 | 1 | 1 | 1 | 1 | 2 | 2 | 2 | 2 | 3 | 3 | 3 |
| Sc | 70 | 78 | 80 | 69 | 71 | 79 | 74 | 83 | 82 | 70 | 82 | 77 |
| V | 354 | 321 | 315 | 279 | 244 | 337 | 344 | 342 | 352 | 338 | 315 | 286 |
| Cr | 667 | 1467 | 1699 | 1038 | 1186 | 2210 | 1031 | 3368 | 1719 | 2847 | 1741 | 1515 |
| Ni | 59 | 90 | 85 | 101 | 86 | 107 | 78 | 88 | 96 | 138 | 106 | 111 |
| Cu | 1·73 | 2·47 | 2·04 | 1·36 | 1·67 | 1·91 | 1·73 | 2·20 | 2·03 | <2·15 | 3·00 | 1·93 |
| Rb* | <0·13 | 0·12 | 0·07 | <0·17 | <0·10 | 0·11 | <0·15 | 0·14 | <0·05 | <0·19 | <0·07 | 0·10 |
| Sr | 69 | 58 | 58 | 68 | 76 | 62 | 56 | 62 | 51 | 58 | 57 | 52 |
| Y | 16·2 | 11·2 | 11·3 | 10·6 | 12·1 | 11·7 | 13·1 | 11·1 | 13·5 | 12·3 | 11·1 | 9·4 |
| Zr | 58 | 34 | 34 | 50 | 64 | 34 | 50 | 35 | 40 | 41 | 32 | 26 |
| Nb | 0·50 | 0·35 | 0·22 | 0·24 | 0·30 | 0·35 | 0·55 | 0·29 | 0·12 | 0·46 | 0·19 | 0·20 |
| Ba | 1·02 | 0·77 | 0·23 | <0·53 | <0·38 | 0·42 | <0·24 | <0·24 | <0·37 | <0·85 | 0·23 | 0·49 |
| La | 3·28 | 2·65 | 2·13 | 4·20 | 4·29 | 2·38 | 2·91 | 1·90 | 2·61 | 2·90 | 1·95 | 1·61 |
| Ce | 11·4 | 7·9 | 7·0 | 10·3 | 13·1 | 6·6 | 9·3 | 7·3 | 8·8 | 8·8 | 7·0 | 5·6 |

(continued)

*Table 4: Continued*

| Xenolith: | NNS08 | | | | | | | | | | | |
|---|---|---|---|---|---|---|---|---|---|---|---|---|
| Grain: | 1 | 1 | 1 | 1 | 1 | 2 | 2 | 2 | 2 | 3 | 3 | 3 |
| Nd | 10·9 | 7·2 | 7·1 | 7·9 | 10·2 | 7·9 | 9·6 | 8·0 | 8·9 | 8·5 | 8·2 | 5·8 |
| Sm | 4·53 | 2·05 | 2·54 | 1·84 | 3·16 | 2·64 | 3·08 | 2·61 | 2·93 | 4·01 | 2·69 | 2·25 |
| Eu | 1·39 | 1·21 | 0·97 | 0·78 | 1·08 | 0·93 | 1·06 | 1·09 | 1·09 | 0·95 | 0·78 | 0·71 |
| Gd | 4·25 | 3·05 | 3·08 | 2·78 | 2·61 | 3·03 | 2·95 | 2·23 | 2·75 | 2·26 | 3·05 | 1·86 |
| Yb | 1·21 | 0·88 | 0·83 | 0·87 | 1·32 | 0·96 | 1·06 | 1·01 | 0·81 | 0·78 | 0·70 | 0·85 |
| Lu | 0·12 | 0·10 | 0·10 | 0·08 | 0·17 | 0·10 | 0·14 | 0·12 | 0·13 | 0·09 | 0·08 | 0·10 |
| Hf | 2·58 | 1·66 | 1·40 | 2·81 | 2·07 | 1·57 | 1·77 | 1·30 | 1·95 | 2·16 | 1·58 | 1·24 |
| Th | 0·18 | 0·13 | 0·09 | 0·25 | 0·13 | 0·06 | 0·13 | 0·04 | <0·06 | <0·11 | <0·02 | 0·07 |
| U | 0·04 | 0·04 | 0·05 | 0·14 | 0·06 | 0·07 | <0·04 | <0·03 | <0·05 | <0·10 | <0·02 | <0·02 |
| Pr | 1·78 | 1·26 | 1·27 | 1·43 | 2·03 | 1·30 | 1·72 | 1·33 | 1·43 | 1·37 | 1·19 | 0·94 |
| Er | 1·78 | 1·24 | 1·03 | 1·40 | 1·43 | 1·29 | 1·49 | 1·30 | 1·40 | 1·32 | 1·01 | 0·92 |
| Ho | 0·73 | 0·45 | 0·50 | 0·42 | 0·45 | 0·51 | 0·61 | 0·42 | 0·51 | 0·54 | 0·46 | 0·35 |
| Tb | 0·67 | 0·47 | 0·46 | 0·48 | 0·45 | 0·41 | 0·44 | 0·40 | 0·46 | 0·48 | 0·48 | 0·33 |
| Dy | 3·76 | 2·65 | 2·54 | 1·58 | 3·31 | 2·51 | 2·50 | 3·12 | 3·04 | 3·19 | 2·54 | 2·16 |
| Tm | 0·14 | 0·12 | 0·15 | 0·13 | 0·16 | 0·13 | 0·14 | 0·16 | 0·13 | 0·26 | 0·13 | 0·08 |

*Because clinopyroxene is packed with melt inclusions, it was difficult to ablate the host mineral free of melt inclusions. Rb is highly incompatible in the clinopyroxene but is present in the melt. It was used as a control to ensure that no entrapped melt was included in the ablated volume.

noted that these analyses are not purely representative of the composition of narrow reaction rims, as the ablation pits are larger than the width of the reaction rim. This is also shown by the transitional major element (especially $TiO_2$) content compared with EMPA data for clinopyroxene cores and rims. Furthermore, if we plot an incompatible trace element concentration against compatible and incompatible elements, clear trends can be observed even in the grain cores that appear to be almost homogeneous with respect to major elements (Fig. 4 and Table 3). The data from the rims fall at the evolved end of these trends. Most incompatible elements display a positive correlation with each other; however, for Y, Yb and Lu this correlation is not so obvious (Fig. 4). More precisely, the concentration of Y shows no systematic change, and the variation of Yb and Lu vs Ce shows a U-shaped pattern, with the lowest values at intermediate Ce contents. In terms of compatible trace elements, Ni shows a clear negative correlation with Ce, whereas Sc and V display a less defined distribution. The Cu content decreases exponentially with increasing Ce concentration (Fig. 4).

The olivine grains are homogeneous in composition in each xenolith, but their compositions differ between xenoliths. Their mg-number ranges from 79 to 85 and the Ni content is between 650 and 1200 ppm. The CaO content ranges from 0·04 to 0·19 wt % with no systematic variation.

The amphibole compositions plot between pargasite and kaersutite with 4·2–4·8 wt % $TiO_2$ (Table 5). The mg-number is between 74 and 77. Their trace element patterns normalized to primitive mantle show positive HFSE and LILE and characteristic negative Pb anomalies (Fig. 5). The breakdown assemblage of amphibole consists of rhönite, Ti-rich diopsidic clinopyroxene, nepheline (Na/K ~ 5·0), olivine (mg-number ~ 84·0) and ilmenite (Table 5, Fig. 2f). The bulk composition of the breakdown assemblage is in good agreement with the amphibole composition in terms of both major and trace elements (Table 5).

## Intercumulus phase assemblages

The alkali feldspar in the intercumulus phase is sanidine with a Na/K ratio of 0·6, the clinopyroxene is diopsidic and the residual glass is highly enriched in $Al_2O_3$ and alkali oxides (Table 6). Relative to the parental melt of the cumulates, the bulk composition of the intercumulus phase assemblage has a slightly elevated $SiO_2$ content (between 50·9 and 55·3 wt %) and very strong enrichment in alkali elements (9·0–15·0 wt % $Na_2O + K_2O$), $Al_2O_3$ (20·8–25·2 wt %) and all incompatible trace elements (Table 7), except for Y and HREE. The $CaO/Al_2O_3$ ratio is very low (0·12–0·37). The REE pattern is remarkably steep, with La/Yb ranging from 21 to 32 (Table 7).

The FeO and MgO contents are low, whereas the mg-numbers are relatively high (49–67).

Downes *et al.* (2004) have studied glass-bearing hornblendite and clinopyroxenite xenoliths entrained in intraplate alkali basalts from Germany and Israel. The bulk compositions of the intercumulus phases compared with the composition of their interstitial glasses have similar total alkali content, but higher concentrations of $SiO_2$ and $Al_2O_3$, and lower concentrations of MgO, CaO, FeO and incompatible trace elements.

## HOMOGENIZATION EXPERIMENTS AND RESULTS

The melting temperatures of the residual glass in the SMIs hosted in olivine range from 1090 to 1170°C. Observation of the onset of glass melting was rather difficult; thus, these values are maximum estimates. Final melting of clinopyroxene and rhönite in SMIs occurred between 1190 and 1250°C, whereas spinel persisted to 1290–1340°C in several cases. Complete dissolution of the gas bubble did not occur in a significant proportion of the studied SMIs, which indicates heterogeneous gas entrapment or partial pressure relaxation in the post-entrapment history of the SMIs. However, decrepitation features were never observed. Despite the relatively slow cooling rate (~300°C/min), partial recrystallization of the homogenized SMIs could not be observed, neither at microscopic scale nor by scanning electron microscope. Homogenization of clinopyroxene-hosted inclusions was not possible, because melting of the host clinopyroxene began before complete homogenization of the SMIs at atmospheric pressure.

Eighteen reheated SMIs were exposed and polished after homogenization and analyzed by electron microprobe. All are at least 15 μm in diameter and were analyzed with at least two or three points to check homogeneity. Twelve inclusions appeared to be completely homogeneous and only data obtained from these were used for interpretation.

Melt inclusion compositions were corrected by adding olivine to achieve a $Kd_{Fe-Mg}$ value of 0·32 that is appropriate for olivines crystallized from basaltic magmas at shallow mantle depths (Ulmer, 1989). This correction accounts for the post-entrapment crystallization of the inclusions (i.e. overgrowth on the inclusions' wall). The normalized compositions of the SMIs are shown in Table 8. They show a trend that represents an interval of parental melt evolution. Relationships between the composition and intragranular textural position (core or rim) could not be evaluated, because in most crystals only one inclusion was measurable. CaO concentration shows a strong negative

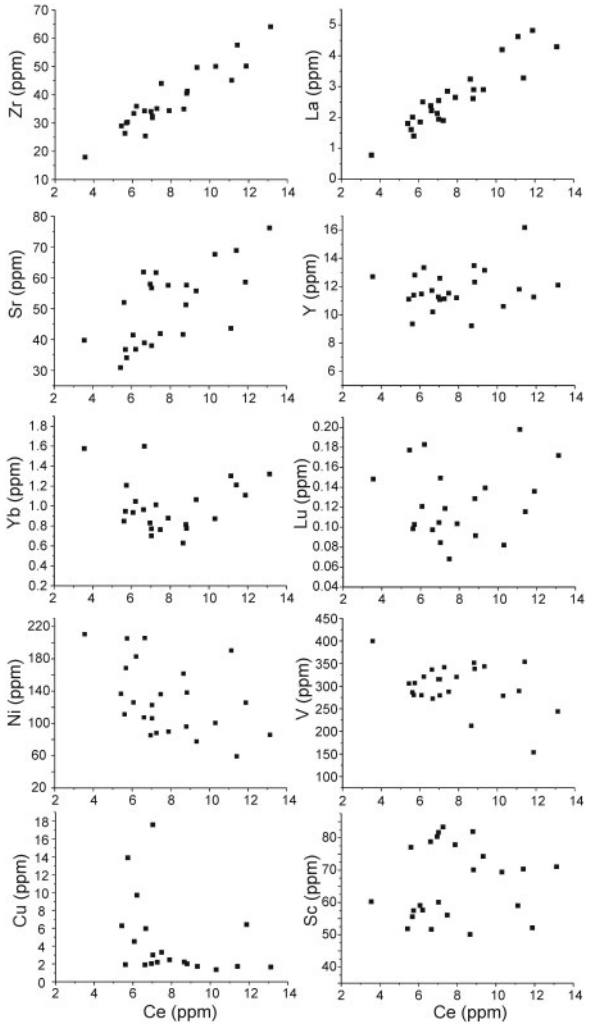


**Fig. 4.** Trace element variation in the rock-forming clinopyroxene as a function of a selected incompatible trace element, Ce.

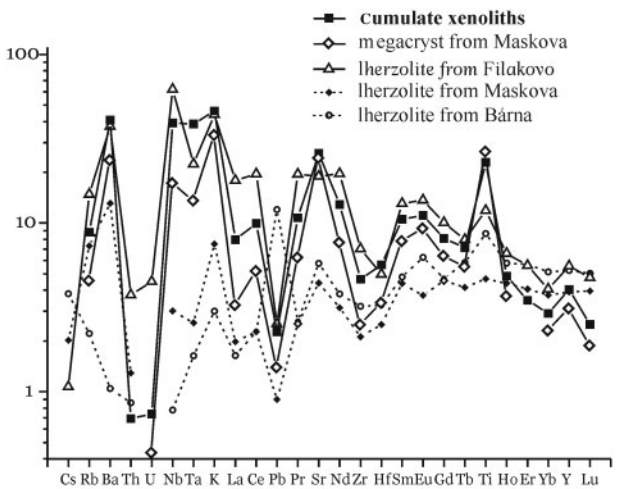


**Fig. 5.** Primitive normalized trace element diagram showing the composition of the xenolith-forming amphiboles. Metasomatic amphiboles found in peridotite xenoliths of the region (Filakovo, Maskova, Bárna) are also shown (Szabó *et al.*, unpublished data).

*Table 5: Average composition of the mineral phases forming the breakdown assemblage of amphibole in xenolith NNS08*

| | Bulk* | amp† (4) | σ | cpx (5) | σ | rh (8) | σ | ne (4) | σ | ol (3) | σ | ilm (1) |
|---|---|---|---|---|---|---|---|---|---|---|---|---|
| $SiO_2$ | 39·7 | 40·8 | 0·3 | 44·5 | 1·5 | 26·9 | 1·8 | 44·2 | 0·3 | 39·4 | 0·3 | 0·09 |
| $TiO_2$ | 4·57 | 4·65 | 0·17 | 4·59 | 0·67 | 10·50 | 1·50 | 0·15 | 0·08 | 0·10 | 0·02 | 51·42 |
| $Al_2O_3$ | 17·0 | 14·4 | 0·4 | 8·6 | 1·7 | 15·7 | 0·3 | 33·4 | 0·4 | 0·02 | 0·02 | 0·27 |
| $Cr_2O_3$ | 0·07 | 0·11 | 0·01 | 0·10 | 0·04 | 0·22 | 0·06 | 0·01 | 0·02 | 0·02 | 0·03 | 0·38 |
| FeO | 7·83 | 7·57 | 0·13 | 5·35 | 0·34 | 17·8 | 1·30 | 0·66 | 0·05 | 15·6 | 0·55 | 34·9 |
| MnO | 0·08 | 0·04 | 0·01 | 0·04 | 0·01 | 0·07 | 0·01 | 0·00 | 0·00 | 0·15 | 0·01 | 0·27 |
| MgO | 13·3 | 14·6 | 0·4 | 12·7 | 0·7 | 15·6 | 0·7 | 0·10 | 0·01 | 45·5 | 0·5 | 11·0 |
| CaO | 10·8 | 11·8 | 0·3 | 23·2 | 0·3 | 11·1 | 0·2 | 1·82 | 0·21 | 0·34 | 0·03 | 0·12 |
| $Na_2O$ | 5·07 | 2·83 | 0·03 | 0·85 | 0·05 | 1·82 | 0·19 | 14·9 | 0·2 | 0·02 | 0·02 | 0·01 |
| $K_2O$ | 1·52 | 1·34 | 0·13 | 0·01 | 0·01 | 0·02 | 0·01 | 4·48 | 0·19 | 0·01 | 0·00 | 0·04 |
| $P_2O_5$ | 0·05 | 0·04 | 0·02 | 0·02 | 0·01 | 0·02 | 0·00 | 0·02 | 0·02 | 0·05 | 0·00 | 0·01 |
| Total | – | 98·12 | | 99·96 | | 99·68 | | 99·68 | | 101·31 | | 98·46 |
| mg-no. | 75·2 | 77·4 | | 80·8 | | 60·9 | | 21·3 | | 83·9 | | 35·9 |
| Sc | 49 | 46 | 6 | 79 | 9 | 63 | 20 | | | | | |
| V | 508 | 452 | 7 | 583 | 85 | 1073 | 84 | | | | | |
| Cr | 402 | 631 | 197 | 544 | 684 | 779 | 396 | | | | | |
| Ni | 196 | 211 | 11 | 115 | 66 | 424 | 69 | | | | | |
| Cu | 34·3 | 6·7 | 1·1 | 5·7 | 0·5 | 5·1 | 2·8 | | | | | |
| Rb | 17·2 | 5·3 | 0·1 | 0·2 | | 0·4 | | | | | | |
| Sr | 248 | 515 | 9 | 111 | 12 | 54 | 29 | | | | | |
| Y | 18·6 | 17·3 | 2·1 | 41·4 | 4·1 | 12·0 | 7·1 | | | | | |
| Zr | 78·1 | 48·8 | 8·1 | 165·9 | 69·5 | 99·3 | 51·3 | | | | | |
| Nb | 32·0 | 26·8 | 2·6 | 10·8 | 9·6 | 32·5 | 2·0 | | | | | |
| Ba | 141 | 269 | 16·6 | 9·6 | 4·2 | 4·0 | | | | | | |
| La | 7·8 | 5·2 | 0·97 | 13·7 | 1·24 | 2·8 | 4·17 | | | | | |
| Ce | 20·6 | 16·7 | 3·2 | 44·2 | 4·0 | 8·2 | 9·1 | | | | | |
| Nd | 16·5 | 16·1 | 1·7 | 36·6 | 3·7 | 7·9 | 8·2 | | | | | |
| Sm | 4·5 | 4·3 | 0·8 | 11·4 | 0·7 | 2·8 | 2·8 | | | | | |
| Eu | 1·59 | 1·71 | 0·18 | 3·30 | 0·29 | 0·88 | 0·80 | | | | | |
| Gd | 4·67 | 4·40 | 0·58 | 9·41 | 1·59 | 2·88 | 1·94 | | | | | |
| Yb | 1·42 | 1·28 | 0·29 | 3·37 | 0·20 | 1·19 | 0·67 | | | | | |
| Lu | 0·18 | 0·17 | 0·06 | 0·34 | 0·07 | 0·25 | 0·12 | | | | | |
| Hf | 2·21 | 1·60 | 0·35 | 4·53 | 1·67 | 2·45 | 2·04 | | | | | |
| Ta | 1·65 | 1·43 | 0·09 | 1·32 | 0·94 | 2·09 | 0·34 | | | | | |
| Pb | 0·82 | 0·34 | 0·10 | 0·72 | | 0·87 | | | | | | |
| Th | 0·64 | 0·06 | 0·01 | 0·41 | | 0·08 | 0·29 | | | | | |
| U | 0·16 | 0·02 | 0·00 | 0·07 | | <0·13 | | | | | | |
| Pr | 3·07 | 2·73 | 0·47 | 7·14 | 0·75 | 1·32 | 1·74 | | | | | |
| Er | 1·80 | 1·53 | 0·63 | 3·31 | 0·24 | 1·21 | 0·81 | | | | | |
| Ho | 0·75 | 0·72 | 0·08 | 1·54 | 0·17 | 0·50 | 0·46 | | | | | |
| Tb | 0·73 | 0·71 | 0·04 | 1·42 | 0·13 | 0·47 | 0·34 | | | | | |

Major elements in wt %; trace elements in ppm.
*Major element data are from EMPA, except for the bulk composition of the breakdown assemblage, which was calculated by averaging sevaral bulk LA-ICPMS analyses (110 μm beam diameter). Numbers in parenthesis show the number of analyses.
†Residual, unaltered part of the amphibole grains.

*Table 6: Average composition of mineral phases and glass (in wt %) in the intercumulus phase assemblage in xenolith NNS07*

| | sanidine (5)* | σ | glass (5) | σ | cpx (3) | σ | Ti-magnetite (1) | apatite (1) |
|---|---|---|---|---|---|---|---|---|
| $SiO_2$ | 63·8 | 0·7 | 52·0 | 0·5 | 48·1 | 0·03 | 0·24 | 1·02 |
| $TiO_2$ | 0·44 | 0·05 | 0·15 | 0·03 | 2·59 | 0·30 | 16·2 | 0·02 |
| $Al_2O_3$ | 18·5 | 0·3 | 29·9 | 0·5 | 4·92 | 0·17 | 0·61 | 0·10 |
| $Cr_2O_3$ | 0·00 | 0·00 | 0·00 | 0·01 | 0·01 | 0·01 | 0·13 | 0·02 |
| FeO | 0·64 | 0·14 | 0·91 | 0·24 | 6·95 | 0·13 | 73·6 | 0·35 |
| MnO | 0·00 | 0·00 | 0·01 | 0·01 | 0·10 | 0·01 | 0·70 | 0·03 |
| MgO | 0·06 | 0·08 | 0·19 | 0·21 | 13·2 | 0·25 | 2·28 | 0·13 |
| CaO | 0·60 | 0·31 | 0·18 | 0·07 | 22·6 | 0·49 | 0·23 | 56·0 |
| $Na_2O$ | 4·28 | 0·89 | 12·87 | 1·13 | 0·75 | 0·03 | 0·04 | 0·09 |
| $K_2O$ | 10·79 | 1·59 | 2·16 | 0·25 | 0·10 | 0·05 | 0·11 | 0·34 |
| $P_2O_5$ | 0·02 | 0·01 | 0·02 | 0·01 | 0·07 | 0·10 | 0·01 | 40·4 |
| Total | 99·19 | | 98·38 | | 99·36 | | 94·11 | 98·56 |

*Number of analyses used for average calculation.

linear correlation with $Al_2O_3$ concentration; thus, the $CaO/Al_2O_3$ ratio is a good tool to describe melt evolution and major element abundances are plotted as a function of $CaO/Al_2O_3$ (Fig. 6).

The results of the LA-ICPMS analyses of single SMIs in olivine are shown in Table 9 and Fig. 7. The trace element content of the SMIs shows a trend similar to that of the major elements. Concentrations of most incompatible trace elements increase strongly with decreasing $CaO/Al_2O_3$ ratio, resulting in a 2–2·5 times enrichment (Fig. 7). Concentrations of Sc and V decrease, and, interestingly, Y is also strongly depleted throughout the melt evolution. In most analyses, HREE were below detection limits. The primitive mantle normalized average composition of the most primitive and most evolved SMIs is shown in Fig. 8. Even the most primitive melt composition shows considerable enrichment in all incompatible elements and a characteristic steep REE pattern.

## DISCUSSION

### Crystallization conditions of the cumulates

The primary goal of this study is to provide an insight into the formation of the olivine-clinopyroxenite cumulate xenoliths and the high-pressure evolution of the parental mafic melts. Therefore, it is important to constrain the *P–T* conditions of these processes and their location in the lithospheric mantle.

Estimation of the pressure and temperature conditions of cumulate formation is possible using our SMI data and the chemical compositions of the xenolith-forming minerals (Table 3). Assuming that the melting temperatures of the daughter phases in the SMIs have not been modified significantly by volatile loss after entrapment, a first-order estimation of crystallization temperature can be achieved based on the heating experiments. The maximum final melting temperatures suggest that clinopyroxene saturation occurred at 1250°C. However, because addition of olivine to the reheated SMIs was necessary to obtain equilibrium melt composition (see above), olivine was probably the first phase to crystallize on the liquidus, implying higher liquidus temperatures. We interpret the presence of the glass (Fig. 3) in the SMIs as a result of incomplete crystallization at depth or melting upon reheating by the host basalt during transport of the xenoliths and quenching after eruption. Initial glass melting temperatures indicate a minimum of 1090°C for the solidus temperature; however, this might be overestimated because of potential H loss from the melt inclusions (Danyushevsky *et al.*, 2002).

Clinopyroxene compositions and the SMI data for olivines (Table 8) allow the application of the clinopyroxene–liquid geothermobarometer of Putirka *et al.* (2003), assuming that the phases represent equilibrium compositions, which is likely because of the slow crystallization and is indicated by the homogeneous major element distributions. The equilibrium melt composition was determined from the homogenized olivine-hosted SMIs. A $CaO/Al_2O_3$ ratio of 0·7 measured in the most primitive melt inclusions suggests that crystallization of significant amounts of clinopyroxene did not happen before their entrapment (see below). Thus the primitive melts (average composition of the three most primitive olivine-hosted homogenized SMIs with the highest $CaO/Al_2O_3$ ratios) were assumed to be in equilibrium with clinopyroxene cores, whereas the most evolved compositions (average composition of the olivine-hosted homogenized SMIs with

*Table 7: Bulk composition of the intercumulus phase assemblages determined by LA-ICPMS in xenolith NNS07*

| | ic1 | ic2 | ic3 | ic4 | ic5 | ic6 | Average (9) |
|---|---|---|---|---|---|---|---|
| $SiO_2$ | 52·2 | 52·5 | 52·2 | 50·9 | 55·2 | 55·3 | 53·1 |
| $TiO_2$ | 1·16 | 1·03 | 0·98 | 1·95 | 1·25 | 1·30 | 1·28 |
| $Al_2O_3$ | 25·2 | 21·7 | 22·4 | 20·8 | 21·0 | 22·2 | 22·2 |
| FeO | 2·81 | 3·42 | 3·64 | 4·02 | 2·86 | 2·29 | 3·17 |
| MnO | 0·02 | 0·05 | 0·05 | 0·04 | 0·03 | 0·02 | 0·04 |
| MgO | 1·52 | 3·57 | 4·17 | 2·93 | 1·81 | 1·32 | 2·55 |
| CaO | 8·12 | 8·06 | 7·38 | 6·55 | 4·17 | 2·57 | 6·14 |
| $Na_2O$ | 6·32 | 6·03 | 5·69 | 6·76 | 6·65 | 7·49 | 6·49 |
| $K_2O$ | 2·71 | 3·57 | 3·47 | 6·03 | 7·03 | 7·54 | 5·06 |
| $P_2O_5$ | 0·20 | 0·48 | 0·43 | 0·68 | 0·39 | 0·32 | 0·42 |
| mg-no. | 49·2 | 65·0 | 67·2 | 56·5 | 53·0 | 50·7 | 56·9 |
| $CaO/Al_2O_3$ | 0·32 | 0·37 | 0·33 | 0·32 | 0·20 | 0·12 | 0·28 |
| $Na_2O + K_2O$ | 9·03 | 9·61 | 9·16 | 12·78 | 13·68 | 15·02 | 11·55 |
| Sc | 6·1 | 11·3 | 8·3 | 14·4 | 7·5 | 4·3 | 8·6 |
| V | 117 | 131 | 92 | 210 | 133 | 70 | 125 |
| Cr | 62 | 25 | 94 | 46 | 12 | 61 | 50 |
| Ni | 109 | 74 | 110 | 71 | 34 | 33 | 72 |
| Cu | 147 | 113 | 183 | 89 | 77 | 72 | 113 |
| Rb | 47 | 76 | 66 | 133 | 200 | 187 | 118 |
| Sr | 819 | 635 | 816 | 442 | 336 | 275 | 554 |
| Y | 12·1 | 18·3 | 11·6 | 23·6 | 19·0 | 15·6 | 16·7 |
| Zr | 118 | 236 | 136 | 274 | 331 | 259 | 226 |
| Nb | 39 | 81 | 84 | 126 | 168 | 136 | 106 |
| Ba | 1552 | 985 | 894 | 709 | 390 | 233 | 794 |
| Cs | 0·35 | 0·99 | 0·88 | 1·65 | 3·11 | 1·75 | 1·45 |
| La | 24 | 41 | 34 | 54 | 47 | 37 | 39 |
| Ce | 40 | 67 | 52 | 87 | 76 | 63 | 64 |
| Nd | 16 | 26 | 18 | 34 | 26 | 20 | 23 |
| Sm | 3·0 | 5·2 | 3·2 | 6·4 | 4·9 | 3·6 | 4·4 |
| Eu | 1·2 | 1·5 | 1·1 | 1·6 | 1·1 | 0·6 | 1·2 |
| Gd | 2·7 | 4·2 | 2·7 | 5·6 | 4·0 | 3·0 | 3·7 |
| Yb | 1·1 | 1·7 | 1·1 | 2·3 | 2·0 | 1·7 | 1·6 |
| Lu | 0·16 | 0·23 | 0·15 | 0·30 | 0·26 | 0·23 | 0·22 |
| Hf | 2·5 | 5·0 | 2·7 | 5·7 | 6·0 | 4·6 | 4·4 |
| Ta | 2·0 | 3·9 | 4·0 | 6·1 | 7·5 | 6·4 | 5·0 |
| Pb | 2·2 | 3·5 | 4·4 | 3·8 | 5·4 | 5·2 | 4·1 |
| Th | 4·2 | 9·0 | 8·1 | 12·6 | 17·1 | 11·0 | 10·3 |
| U | 1·2 | 3·0 | 2·7 | 4·4 | 6·0 | 3·8 | 3·5 |
| Pr | 4·1 | 6·8 | 4·9 | 8·7 | 7·3 | 5·7 | 6·3 |
| Er | 1·2 | 1·7 | 1·1 | 2·4 | 2·0 | 1·6 | 1·7 |
| Ho | 0·45 | 0·71 | 0·44 | 0·92 | 0·74 | 0·60 | 0·64 |
| Tb | 0·42 | 0·68 | 0·41 | 0·84 | 0·60 | 0·50 | 0·57 |
| La/Yb | 22·7 | 24·6 | 31·5 | 23·8 | 22·9 | 21·5 | 24·5 |
| Sr/Y | 67·8 | 34·8 | 70·5 | 18·8 | 17·7 | 17·6 | 37·8 |
| Zr/Hf | 47·1 | 47·1 | 50·7 | 48·3 | 54·9 | 56·1 | 50·7 |
| Nb/Ta | 19·9 | 20·8 | 21·2 | 20·8 | 22·4 | 21·3 | 21·1 |

Major elements in wt %; trace elements in ppm.

$CaO/Al_2O_3 \leq 0{\cdot}45$) were thought to be in equilibrium with reaction rims of the clinopyroxenes. This assumption has some uncertainties, especially for the estimates based on the clinopyroxene core compositions, as these probably re-equilibrated to some extent with later residual melts via diffusion. The method is, however, more sensitive to variation in the jadeite component of clinopyroxene than to the variability in the equilibrium melt composition. For the calculations of the clinopyroxene components, the method of Putirka (1999) was used. Calculated pressure and temperature values are shown in Table 3 along with the clinopyroxene compositions. The average uncertainty of the method is $\pm 33^\circ$C and $\pm 1{\cdot}7$ kbar (Putirka *et al.*, 2003). This might be higher for the *P–T* estimations based on clinopyroxene cores, because of the uncertainty in the equilibrium melt composition. The estimated crystallization temperature for clinopyroxene cores ranges from 1185 to 1200°C. This is in good agreement with the temperature data for clinopyroxene final melting in the olivine-hosted SMIs but lower than the clinopyroxene saturation temperatures obtained by pMELTS modelling (see below). The calculated crystallization pressures for clinopyroxene cores are between 10 and 12 kbar. The reaction rims indicate lower crystallization temperatures (1120–1150°C) than the cores; however, the estimated pressure values are indistinguishable within the error of the method (8·7–12·0 kbar). These values suggest that crystallization of the cumulate bodies happened at a depth of ~ 29–38 km, in the uppermost lithospheric mantle close to the Moho (Huismans *et al.*, 2001) without significant ascent in the recorded cooling and crystallization interval.

We estimated the oxygen fugacity during crystallization using the method of Ballhaus *et al.* (1991) based on the composition of small Cr-spinel inclusions in olivine. The values scatter between QFM + 1·0 and QFM + 1·23 log units (where QFM is the quartz–fayalite–magnetite buffer).

## Do the melt inclusions represent the composition of the parental melt?

The physical conditions of crystallization of the cumulate bodies near the Moho and their cooling rates are different from those of basaltic volcanic systems from which most previous studies of SMIs in olivine have been reported. Most of these earlier studies were carried out on compositionally zoned olivine phenocrysts formed by fractional crystallization in volcanic systems. In our case the homogeneous composition of the host olivine crystals indicates equilibrium crystallization accompanied by slow cooling characteristic of underplated igneous bodies. Iron loss, suggested for melt inclusions hosted in magmatic olivine phenocrysts (Danyushevsky *et al.*, 2000), may not be significant here because of the equilibrium crystallization of the host olivine. On the other hand, the FeO/MgO ratio in the SMIs is considered to be identical to the latest melt composition, which was in equilibrium with the host olivine. In this scenario, it is assumed that the SMIs maintain

*Table 8: Major element composition of the homogenized melt inclusions in olivine of xenolith NNS07 analyzed by EPMA (in wt %)*

| Inclusion: | 01 | 02 | 03 | 04 | 05 | 06 | 07 | 08 | 09 | 10 | 11 | 12 |
|---|---|---|---|---|---|---|---|---|---|---|---|---|
| $SiO_2$ | 48·7 | 47·1 | 46·0 | 45·1 | 45·8 | 44·8 | 46·5 | 47·2 | 45·8 | 47·3 | 43·8 | 45·1 |
| $Al_2O_3$ | 22·7 | 19·9 | 22·7 | 20·9 | 20·9 | 19·2 | 20·5 | 19·3 | 18·8 | 18·4 | 18·1 | 18·0 |
| $TiO_2$ | 2·04 | 2·09 | 2·43 | 2·66 | 2·64 | 3·12 | 4·37 | 3·18 | 3·04 | 2·76 | 2·36 | 2·13 |
| $Cr_2O_3$ | 0·005 | 0·001 | 0·014 | 0·002 | 0·035 | 0·012 | 0·006 | 0·037 | 0·003 | 0·023 | 0·012 | 0·004 |
| FeO | 4·80 | 6·11 | 6·40 | 6·69 | 6·60 | 8·59 | 7·04 | 5·80 | 8·45 | 8·55 | 8·49 | 10·01 |
| MgO | 4·02 | 4·95 | 5·30 | 5·53 | 5·33 | 6·81 | 5·73 | 4·61 | 6·71 | 6·87 | 6·67 | 7·88 |
| MnO | 0·10 | 0·09 | 0·10 | 0·10 | 0·12 | 0·16 | 0·10 | 0·09 | 0·12 | 0·10 | 0·12 | 0·17 |
| CaO | 7·17 | 10·50 | 9·04 | 9·38 | 9·47 | 8·73 | 7·64 | 10·80 | 8·32 | 8·42 | 12·28 | 10·37 |
| $K_2O$ | 4·22 | 2·86 | 2·83 | 3·09 | 3·04 | 3·16 | 3·36 | 2·86 | 2·73 | 2·74 | 2·72 | 2·57 |
| $Na_2O$ | 5·30 | 4·78 | 4·63 | 4·81 | 4·05 | 4·36 | 4·66 | 4·59 | 4·09 | 4·12 | 3·50 | 3·46 |
| $P_2O_5$ | 0·63 | 0·47 | 0·39 | 0·33 | 0·32 | 0·35 | 0·31 | 0·38 | 0·40 | 0·23 | 0·26 | 0·23 |
| NiO | 0·012 | 0·012 | 0·018 | 0·000 | 0·000 | 0·005 | 0·002 | 0·028 | 0·013 | 0·000 | 0·000 | 0·022 |
| Total | 99·76 | 98·84 | 99·78 | 98·62 | 98·25 | 99·30 | 100·27 | 98·90 | 98·46 | 99·53 | 98·37 | 99·97 |
| Added host (wt %) | 0 | 1 | 8 | 7 | 6 | 13 | 10 | 5 | 14 | 14 | 12 | 15 |
| $CaO/Al_2O_3$ | 0·32 | 0·53 | 0·40 | 0·45 | 0·45 | 0·45 | 0·37 | 0·56 | 0·44 | 0·46 | 0·68 | 0·58 |
| $Na_2O + K_2O$ | 9·52 | 7·64 | 7·45 | 7·89 | 7·09 | 7·53 | 8·02 | 7·45 | 6·82 | 6·86 | 6·22 | 6·03 |

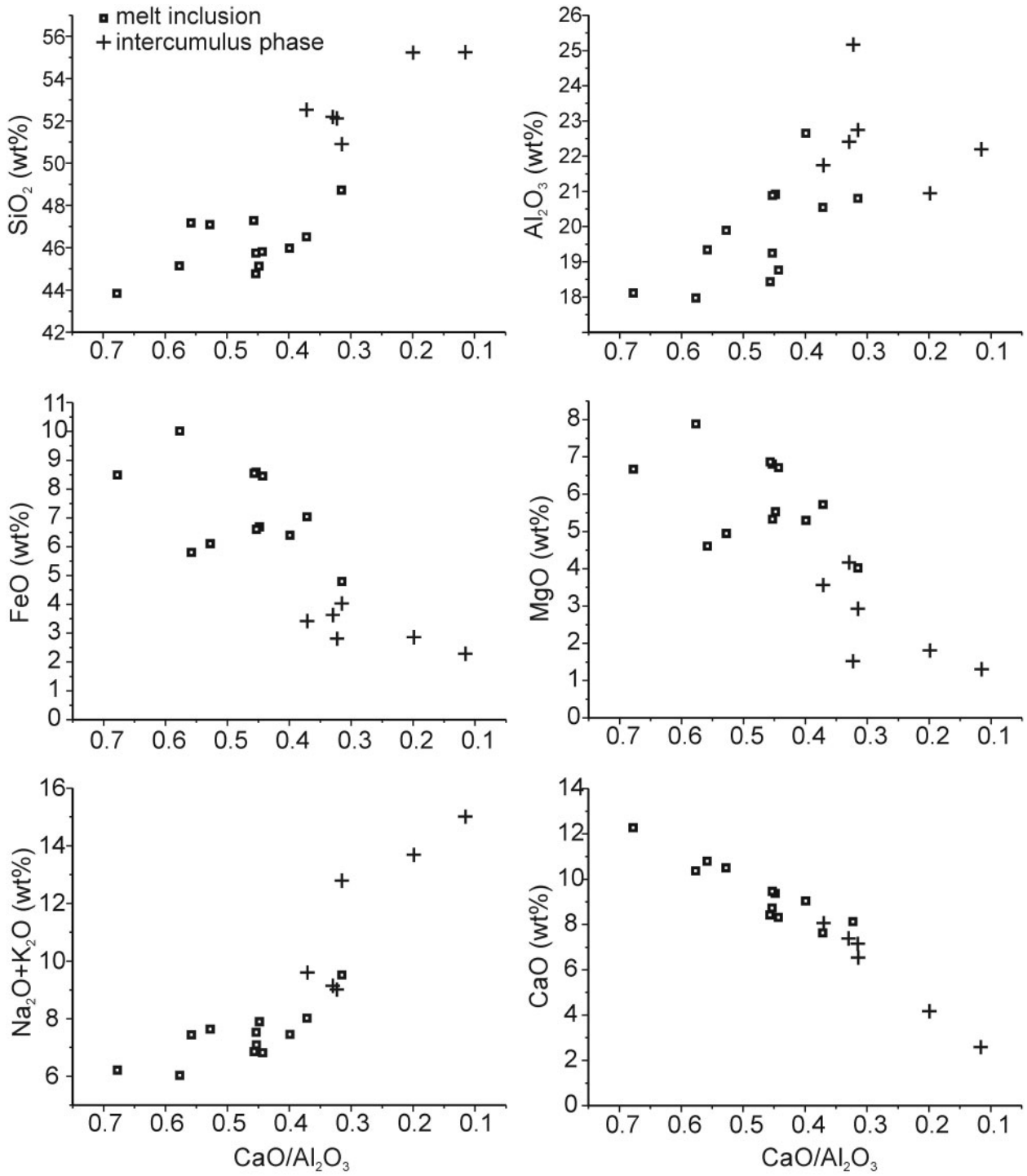


**Fig. 6.** Major element variation diagrams for homogenized SMIs (□) as a function of $CaO/Al_2O_3$ ratio. The bulk composition of the analyzed intercumulus phase (+) is also shown, forming a continuous trend towards low $CaO/Al_2O_3$ ratios.

equilibrium with the olivine host composition, which maintains equilibrium with the residual melt. Non-representative remelting of olivine crystallized on the inclusion walls during the reheating experiments or crystallization on the walls upon quenching can also induce significant modifications in the melt compositions. However, these can be properly corrected for, using Fe/Mg exchange equilibria between the host olivine and the entrapped melt (Table 8). In contrast, all those major and trace elements that are incompatible in the host olivine

*Table 9: Results of LA-ICPMS analyses of individual unheated melt inclusions in olivine*

| Xenolith: | NNS07 | | | | | | | | | | | | | | | | | |
|---|---|---|---|---|---|---|---|---|---|---|---|---|---|---|---|---|---|---|
| Inclusion: | 01 | σ (%) | 02 | σ (%) | 03 | σ (%) | 04 | σ (%) | 05 | σ (%) | 06 | σ (%) | 07 | σ (%) | 08 | σ (%) | 09 | σ (%) |
| $Al_2O_3$ | 16·91 | 1·0 | 17·18 | 1·2 | 19·86 | 1·6 | 19·27 | 1·5 | 17·86 | 2·0 | 16·39 | 1·3 | 17·60 | 1·4 | 19·50 | 1·4 | 18·14 | 1·2 |
| CaO | 8·72 | 5·9 | 11·90 | 4·5 | 11·96 | 9·8 | 10·59 | 11·6 | 10·07 | 28·1 | 10·98 | 6·3 | 10·28 | 6·0 | 10·77 | 4·5 | 7·55 | 6·2 |
| $Na_2O$ | 5·18 | 1·0 | 4·51 | 1·3 | 5·17 | 1·8 | 5·21 | 1·6 | 5·24 | 2·3 | 4·67 | 1·4 | 4·98 | 1·5 | 5·14 | 1·5 | 5·50 | 1·2 |
| $K_2O$ | 2·22 | 1·1 | 1·78 | 1·4 | 1·64 | 2·5 | 1·94 | 2·2 | 1·82 | 4·0 | 1·73 | 1·7 | 1·94 | 1·7 | 1·99 | 1·5 | 2·65 | 1·3 |
| P | 803 | 32·5 | 926 | 19·6 | <2327 | | 1522 | 56·6 | <4314 | | 1046 | 28·7 | 1654 | 16·3 | 1716 | 11·4 | 2297 | 10·1 |
| V | 387 | 4·4 | 386 | 4·4 | 599 | 7·3 | 523 | 7·7 | 420 | 15·9 | 409 | 5·6 | 337 | 5·9 | 302 | 4·9 | 388 | 4·6 |
| Cr | 673 | 15·9 | 426 | 18·3 | 1772 | 16·1 | 639 | 27·5 | 1838 | 33·2 | 776 | 16·0 | 435 | 23·0 | 308 | 21·0 | 556 | 15·8 |
| Cu | 789 | 7·1 | 283 | 12·4 | 711 | 16·5 | 969 | 14·6 | <3127 | | 886 | 9·3 | 1256 | 7·5 | 389 | 10·4 | 1474 | 5·6 |
| Rb | 28 | 11·6 | 23 | 13·6 | 31 | 25·4 | 41 | 22·0 | 53 | 32·5 | 29 | 17·2 | 33 | 15·3 | 34 | 11·5 | 49 | 10·2 |
| Sr | 588 | 2·5 | 534 | 2·0 | 578 | 5·5 | 529 | 5·5 | 511 | 9·7 | 500 | 3·8 | 708 | 3·1 | 845 | 2·4 | 711 | 2·6 |
| Y | 14 | 17·8 | 18 | 14·7 | 25 | 18·2 | 16 | 30·6 | <198 | | 22 | 17·2 | 18 | 18·3 | 20 | 12·9 | 18 | 15·3 |
| Zr | 151 | 6·5 | 148 | 7·1 | 218 | 12·1 | 142 | 14·6 | 129 | 27·4 | 149 | 9·4 | 222 | 7·2 | 225 | 5·6 | 182 | 6·5 |
| Nb | 47 | 8·9 | 33 | 11·1 | 56 | 17·6 | 37 | 21·1 | 29 | 51·7 | 41 | 13·2 | 43 | 12·1 | 40 | 9·7 | 55 | 8·7 |
| Ba | 480 | 6·3 | 302 | 8·3 | 480 | 14·2 | 283 | 19·5 | 203 | 34·3 | 377 | 10·3 | 320 | 10·3 | 414 | 7·0 | 578 | 6·3 |
| Cs | <6·0 | | <7·8 | | <17·9 | | <9·3 | | <13·8 | | <5·7 | | <11·5 | | <9·3 | | <6·8 | |
| La | 21 | 11·0 | 15 | 13·8 | 22 | 24·9 | 19 | 26·7 | 18 | 43·2 | 23 | 15·5 | 22 | 14·8 | 26 | 10·5 | 26 | 11·2 |
| Ce | 42 | 8·2 | 34 | 9·3 | 61 | 14·5 | 24 | 22·8 | 42 | 29·4 | 48 | 10·4 | 54 | 9·2 | 58 | 6·9 | 65 | 6·9 |
| Nd | 21 | 26·7 | 26 | 24·8 | 53 | 35·5 | <77·5 | | 95 | 42·9 | 32 | 30·3 | 54 | 21·5 | 41 | 18·8 | 28 | 23·0 |
| Sm | 12·4 | 37·9 | 10·9 | 40·2 | <28·5 | | <22·6 | | <50·7 | | 19·2 | 37·3 | <21·0 | | 6·6 | 54·6 | 6·5 | 59·3 |
| Eu | <5·3 | | 2·5 | 40·9 | <2·1 | | <8·2 | | <10·7 | | 3·1 | 56·5 | <9·6 | | 3·8 | 38·1 | 4·4 | 34·6 |
| Gd | <20·2 | | 14·7 | 34·0 | <26·00 | | <44·0 | | <38·0 | | 14·1 | 44·0 | 10·12 | 54·1 | <18·2 | | <23·5 | |
| Yb | <5·19 | | <4·30 | | 2·25 | 58·4 | <8·53 | | <4·88 | | <3·95 | | <4·27 | | <4·25 | | <6·07 | |
| Lu | <1·66 | | <1·26 | | <1·49 | | <3·08 | | <6·34 | | <2·94 | | <2·47 | | <3·49 | | <2·81 | |
| Hf | <8·23 | | 4·34 | 70·6 | <6·14 | | <16·70 | | <12·76 | | <9·42 | | <8·45 | | <7·96 | | <9·83 | |
| Ta | 1·35 | 39·9 | 1·29 | 50·3 | 2·17 | 68·7 | <4·14 | | <7·25 | | 2·57 | 46·1 | 2·03 | 54·0 | 2·54 | 34·6 | 3·06 | 32·6 |
| Pb | <9·58 | | <6·05 | | <9·97 | | <16·06 | | <19·22 | | <11·49 | | <10·21 | | <12·91 | | <7·13 | |
| Th | <3·14 | | 1·22 | 50·8 | <3·20 | | <5·32 | | <7·64 | | <3·62 | | 1·53 | 61·1 | 1·01 | 56·3 | 3·43 | 35·3 |
| U | 1·05 | 55·4 | <2·19 | | <3·15 | | <5·45 | | <6·79 | | <3·34 | | <3·47 | | <2·91 | | <2·49 | |
| Pr | 5·0 | 18 | 4·2 | 22 | 6·5 | 41 | <18·6 | | <17·5 | | 4·9 | 30 | 6·6 | 24 | 6·8 | 18 | 6·0 | 21 |
| Er | <5·91 | | <4·40 | | <6·05 | | <12·27 | | <20·79 | | 4·86 | 76·0 | <11·45 | | <13·20 | | 2·72 | 63·8 |
| Ho | <1·89 | | <1·78 | | <2·31 | | <4·81 | | <5·81 | | <2·54 | | <3·30 | | <3·62 | | <2·10 | |
| Tb | <1·71 | | <1·51 | | <2·52 | | <5·50 | | <6·71 | | <2·73 | | <2·17 | | <2·93 | | <1·71 | |

| Xenolith: | NNS07 | | | | | | | | | | | | | | | | | |
|---|---|---|---|---|---|---|---|---|---|---|---|---|---|---|---|---|---|---|
| Inclusion: | 10 | σ (%) | 11 | σ (%) | 12 | σ (%) | 13 | σ (%) | 14 | σ (%) | 15 | σ (%) | 16 | σ (%) | 17 | σ (%) | 18 | σ (%) |
| $Al_2O_3$ | 14·86 | 1·1 | 17·57 | 1·1 | 18·22 | 1·3 | 19·88 | 1·1 | 16·89 | 1·2 | 17·23 | 1·7 | 18·69 | 1·3 | 21·07 | 1·2 | 20·13 | 2·6 |
| CaO | 10·59 | 5·2 | 7·55 | 6·8 | 10·30 | 3·2 | 10·60 | 2·1 | 9·90 | 2·3 | 6·38 | 5·3 | 10·89 | 2·8 | 14·14 | 3·8 | 13·79 | 15·9 |
| $Na_2O$ | 4·42 | 1·2 | 5·62 | 1·1 | 4·95 | 1·3 | 5·03 | 1·2 | 4·56 | 1·2 | 5·64 | 1·7 | 4·81 | 1·4 | 4·88 | 1·2 | 4·63 | 2·1 |
| $K_2O$ | 1·75 | 1·4 | 2·43 | 1·3 | 2·06 | 1·3 | 2·24 | 1·2 | 2·32 | 1·2 | 2·88 | 1·7 | 2·13 | 1·3 | 1·54 | 1·4 | 1·65 | 1·7 |
| P | <512 | | 1328 | 17·8 | 1152 | 10·8 | 1080 | 5·7 | 1982 | 4·3 | 2033 | 9·2 | 957 | 10·7 | 674 | 26·4 | 873 | 27·7 |
| V | 483 | 3·9 | 403 | 4·8 | n.d. | 0·0 | n.d. | 0·0 | n.d. | 0·0 | n.d. | 0·0 | n.d. | 0·0 | 553 | 3·5 | 275 | 15·3 |
| Cr | 690 | 14·7 | 814 | 13·9 | 661 | 12·1 | 487 | 8·3 | 685 | 7·4 | 869 | 13·4 | 526 | 11·9 | 516 | 15·4 | 1418 | 20·8 |

(continued)

*Table 9: Continued*

| Xenolith: | NNS07 | | | | | | | | | | | | | | | | | | | |
|---|---|---|---|---|---|---|---|---|---|---|---|---|---|---|---|---|---|---|---|---|
| Inclusion: | 10 | σ (%) | 11 | σ (%) | 12 | σ (%) | 13 | σ (%) | 14 | σ (%) | 15 | σ (%) | 16 | σ (%) | 17 | σ (%) | 18 | σ (%) |
| Cu | 534 | 8·6 | 1395 | 6·1 | 564 | 7·7 | 196 | 7·9 | 1079 | 3·7 | 1411 | 6·4 | 515 | 6·5 | 148 | 16·9 | 353 | 12·2 |
| Rb | 24 | 14·5 | 36 | 13·1 | 41 | 8·9 | 44 | 5·2 | 40 | 5·8 | 61 | 9·6 | 38 | 7·4 | 20 | 13·4 | 28 | 14·7 |
| Sr | 528 | 2·8 | 748 | 2·6 | 478 | 2·6 | 630 | 1·6 | 778 | 1·6 | 834 | 2·8 | 616 | 2·1 | 648 | 2·4 | 572 | 3·8 |
| Y | 25 | 14·7 | 14 | 19·8 | 19 | 12·2 | 26 | 6·2 | 23 | 6·9 | 15 | 17·2 | 21 | 9·5 | 25 | 11·4 | 23 | 23·6 |
| Zr | 146 | 7·3 | 175 | 7·1 | 167 | 6·0 | 159 | 3·8 | 229 | 3·4 | 318 | 5·8 | 140 | 5·3 | 116 | 7·2 | 51 | 34·6 |
| Nb | 37 | 10·0 | 56 | 9·1 | 38 | 9·5 | 48 | 5·1 | 64 | 4·7 | 77 | 8·7 | 25 | 9·3 | 25 | 12·0 | 29 | 13·3 |
| Ba | 271 | 8·8 | 539 | 6·8 | 415 | 6·1 | 381 | 3·9 | 571 | 3·5 | 588 | 6·8 | 350 | 5·4 | 247 | 8·5 | 330 | 8·8 |
| Cs | <8·6 | | <10·8 | | 1·06 | 41·5 | 0·45 | 40·2 | 0·41 | 43·9 | 1·87 | 39·6 | 0·37 | 69·9 | <10·9 | | <6·8 | |
| La | 17 | 13·2 | 33 | 10·3 | 24 | 10·1 | 25 | 5·9 | 42 | 4·9 | 47 | 9·4 | 22 | 8·5 | 15 | 12·8 | 19 | 19·4 |
| Ce | 50 | 8·0 | 59 | 7·6 | 53 | 6·5 | 56 | 3·9 | 79 | 3·6 | 81 | 7·0 | 48 | 5·7 | 32 | 8·9 | 33 | 16·2 |
| Nd | 20 | 25·0 | 36 | 21·5 | 41 | 16·2 | 28 | 11·6 | 38 | 10·7 | 33 | 23·4 | 34 | 14·0 | 37 | 17·9 | 24 | 41·9 |
| Sm | <16·0 | | <13·7 | | 4·8 | 56·7 | 7·6 | 23·9 | 10·4 | 22·5 | 5·8 | 61·5 | 6·8 | 34·4 | 9·1 | 41·4 | <15·1 | |
| Eu | <4·7 | | <6·7 | | 2·7 | 39·4 | 3·5 | 19·5 | 2·8 | 23·4 | 6·0 | 32·8 | 2·8 | 29·0 | 2·7 | 33·5 | <5·1 | |
| Gd | 2·6 | | 7·1 | 51·0 | 9·8 | 36·9 | 7·3 | 26·0 | 9·4 | 23·7 | 5·6 | 64·8 | 6·8 | 34·4 | 10·0 | 36·6 | <14·4 | |
| Yb | <5·84 | | <4·12 | | <7·66 | | 2·70 | 40·4 | <6·27 | | <3·77 | | <4·27 | | <7·01 | | <3·81 | |
| Lu | <2·72 | | <1·40 | | <1·26 | | 0·30 | 50·0 | <0·78 | | <1·55 | | <0·47 | | <2·61 | | <1·18 | |
| Hf | 1·66 | | <5·10 | | 4·845 | 38·2 | 3·365 | 26·9 | 4·47 | 24·4 | 9·46 | 34·0 | 3·81 | 33·8 | 1·54 | 376·7 | <11·09 | |
| Ta | 1·02 | | 1·69 | 60·3 | 2·58 | 27·4 | 2·80 | 15·6 | 2·77 | 16·6 | 4·50 | 27·0 | 1·81 | 25·4 | 1·24 | 41·8 | 1·51 | 37·5 |
| Pb | <9·10 | | <7·37 | | <1·53 | | 2·94 | 21·0 | 1·94 | 28·3 | 4·04 | 39·5 | 2·32 | 37·2 | <8·78 | | 1·67 | 96·3 |
| Th | 1·46 | 45·4 | 4·08 | 31·4 | 2·77 | 25·5 | 3·94 | 12·7 | 4·66 | 12·4 | 6·23 | 21·9 | 2·70 | 20·2 | <6·13 | | <2·19 | |
| U | <3·60 | | <2·45 | | 0·73 | 47·8 | 1·50 | 19·3 | <0·67 | | 2·85 | 30·5 | 1·33 | 27·4 | <1·97 | | 1·66 | 64·9 |
| Pr | 4·6 | 19 | 7·4 | 19 | 6·3 | 16 | 5·5 | 11 | 7·6 | 10 | 12·7 | 15 | 7·1 | 13 | 2·4 | 24 | 4·8 | 36 |
| Er | <7·24 | | 4·22 | 58·3 | 2·23 | 64·0 | 2·34 | 37·7 | 1·32 | 56·6 | <8·08 | | <4·02 | | <6·47 | | <7·63 | |
| Ho | <1·91 | | <2·06 | | n.d. | | n.d. | | n.d. | | n.d. | | n.d. | | <2·28 | | <2·39 | |
| Tb | 0·31 | | <1·72 | | 1·11 | 43·2 | 1·25 | 24·4 | 0·98 | 28·8 | 1·21 | 53·7 | 1·03 | 35·4 | <3·89 | | <2·50 | |

| Xenolith: | NNS07 | | | | NNS08 | | | | | | | | | | | |
|---|---|---|---|---|---|---|---|---|---|---|---|---|---|---|---|---|
| Inclusion: | 19 | σ (%) | 20 | σ (%) | 01 | σ (%) | 02 | σ (%) | 03 | σ (%) | 04 | σ (%) | 05 | σ (%) | 06 | σ (%) |
| $Al_2O_3$ | 20·63 | 1·0 | 15·73 | 1·2 | 19·87 | 1·4 | 20·00 | 1·0 | 20·00 | 1·2 | 21·67 | 1·1 | 21·56 | 1·6 | 21·46 | 1·1 |
| CaO | 12·84 | 2·7 | 9·78 | 4·3 | 15·96 | 4·5 | 10·74 | 2·9 | 9·35 | 2·4 | 10·18 | 2·8 | 10·29 | 6·6 | 12·46 | 2·0 |
| $Na_2O$ | 4·95 | 1·0 | 4·58 | 1·3 | 4·22 | 1·4 | 2·98 | 1·0 | 3·52 | 1·2 | 4·46 | 1·1 | 4·64 | 1·7 | 4·91 | 1·1 |
| $K_2O$ | 1·73 | 1·1 | 2·10 | 1·4 | 1·54 | 1·7 | 3·02 | 1·0 | 2·39 | 1·2 | 3·26 | 1·1 | 3·02 | 1·8 | 2·03 | 1·1 |
| P | 869 | 20·5 | 1281 | 12·4 | 222 | | 2743 | 4·4 | 1994 | 4·0 | 2011 | 5·8 | 1490 | 14·9 | 1212 | 5·9 |
| V | 521 | 2·2 | 305 | 4·4 | 604 | 4·1 | 422 | 2·7 | 304 | 2·5 | 232 | 3·4 | 364 | 6·5 | n.d. | 0·0 |
| Cr | 460 | 9·7 | 737 | 10·6 | 676 | 14·5 | 1694 | 5·2 | 723 | 5·9 | 668 | 8·2 | 489 | 26·1 | 595 | 8·2 |
| Cu | 754 | 4·5 | 573 | 7·8 | 629 | 9·7 | 154 | 10·7 | 149 | 7·9 | 183 | 9·0 | 169 | 23·9 | 305 | 6·8 |
| Rb | 26 | 7·5 | 55 | 8·3 | 16 | 18·9 | 54 | 5·8 | 48 | 4·6 | 63 | 4·9 | 38 | 15·7 | 43 | 5·7 |
| Sr | 596 | 1·7 | 534 | 2·6 | 636 | 2·9 | 865 | 1·6 | 651 | 1·6 | 839 | 1·6 | 944 | 3·2 | 533 | 1·8 |
| Y | 29 | 6·3 | 21 | 11·9 | 37 | 11·4 | 18 | 9·1 | 19 | 6·5 | 19 | 7·9 | 12 | 25·2 | 25 | 6·9 |
| Zr | 135 | 4·1 | 181 | 5·7 | 117 | 8·8 | 236 | 3·7 | 168 | 3·3 | 187 | 3·7 | 180 | 9·4 | 156 | 4·1 |

(continued)

*Table 9: Continued*

| Xenolith: | NNS07 | | | | NNS08 | | | | | | | | | | | |
|---|---|---|---|---|---|---|---|---|---|---|---|---|---|---|---|---|
| Inclusion: | 19 | σ (%) | 20 | σ (%) | 01 | σ (%) | 02 | σ (%) | 03 | σ (%) | 04 | σ (%) | 05 | σ (%) | 06 | σ (%) |
| Nb | 39 | 5·6 | 51 | 7·9 | 40 | 11·2 | 52 | 5·7 | 43 | 4·7 | 61 | 4·8 | 99 | 9·4 | 32 | 6·7 |
| Ba | 284 | 4·9 | 450 | 6·2 | 405 | 7·9 | 740 | 3·5 | 438 | 3·4 | 673 | 3·3 | 610 | 8·6 | 290 | 4·8 |
| Cs | <1·76 | | <3·43 | | <8·45 | | <3·69 | | 0·13 | 69·8 | 0·66 | 35·5 | <4·66 | | 0·57 | 37·2 |
| La | 15 | 8·2 | 25 | 9·8 | 16 | 14·7 | 33 | 6·2 | 34 | 4·5 | 38 | 5·2 | 32 | 14·0 | 27 | 6·2 |
| Ce | 43 | 4·6 | 52 | 6·7 | 60 | 7·8 | 68 | 4·2 | 65 | 3·3 | 69 | 3·8 | 71 | 9·3 | 53 | 4·3 |
| Nd | 31 | 11·7 | 21 | 24·2 | 31 | 20·6 | 31 | 13·5 | 30 | 9·9 | 37 | 10·7 | 29 | 32·8 | 35 | 11·4 |
| Sm | 6·3 | 26·6 | 6·9 | 47·9 | <15·3 | | <20·2 | | 7·6 | 21·8 | 3·8 | 41·6 | 13·3 | 54·6 | 7·1 | 28·1 |
| Eu | 2·4 | 24·8 | 2·0 | 48·5 | 4·8 | 43·8 | 1·3 | 46·4 | 2·6 | 21·3 | 2·2 | 31·2 | <8·5 | | 3·0 | 23·9 |
| Gd | 9·8 | 18·1 | <23·9 | | <35·3 | | <24·9 | | 6·3 | 25·3 | 4·8 | 41·8 | <20·6 | | 4·6 | 35·4 |
| Yb | <2·79 | | <2·41 | | <2·08 | | <3·69 | | 3·07 | 32·6 | 1·19 | 49·2 | <3·53 | | 4·96 | 32·8 |
| Lu | <0·81 | | <1·57 | | <1·71 | | <3·93 | | 0·13 | 69·4 | <5·32 | | <1·50 | | 0·36 | 49·5 |
| Hf | 0·9 | | 4·08 | 53·5 | <10·32 | | 8·49 | 23·2 | 3·59 | 26·3 | 5·11 | 27·1 | 4·81 | 70·2 | 5·35 | 23·0 |
| Ta | 2·05 | 18·8 | 1·71 | 39·1 | 2·13 | 38·4 | 3·51 | 18·8 | 2·93 | 15·2 | 1·98 | 22·9 | 5·42 | 34·7 | 2·28 | 18·9 |
| Pb | 1·66 | | 2·65 | 50·8 | <10·96 | | 1·92 | 39·7 | 2·05 | 26·1 | 2·13 | 36·8 | <6·92 | | 2·04 | 28·7 |
| Th | 0·58 | | 5·89 | 22·4 | 1·72 | 44·2 | 4·98 | 16·0 | 2·41 | 17·4 | 4·83 | 14·8 | <9·84 | | 3·45 | 14·9 |
| U | <2·25 | | 1·41 | 47·5 | <2·77 | | 1·10 | 39·0 | 0·32 | 56·1 | 1·25 | 32·4 | 1·01 | 73·7 | 0·75 | 30·2 |
| Pr | 5·7 | 11 | 7·0 | 16 | 5·7 | 25 | 8·0 | 11 | 7·3 | 8 | 8·6 | 9 | 8·5 | 24 | 7·3 | 10 |
| Er | <4·33 | | <7·64 | | <4·91 | | 3·58 | 35·5 | 2·24 | 30·7 | 2·68 | 31·8 | <6·16 | | 2·63 | 37·5 |
| Ho | 0·50 | 40·0 | <2·46 | | <3·86 | | <5·48 | | 0·37 | 39·8 | 1·14 | 27·8 | 0·53 | 110·4 | n.d. | |
| Tb | 0·97 | 55·4 | 0·76 | 59·4 | 2·44 | 37·1 | <4·20 | | 0·55 | 30·9 | 1·20 | 24·9 | <2·18 | | 0·62 | 37·8 |

Major elements in wt %; trace elements in ppm.

and have low diffusion coefficients are likely to be representative of the original melt composition. As data from inclusions smaller than 15 μm were not considered and crystallization should be slow, boundary layer effects are unlikely to play a significant role (Kuzmin & Sobolev, 2004).

## Composition of the parental melt

We estimated the composition of the parental melt by fitting trend lines to the SMI compositions on major and trace element plots and taking the values at a $CaO/Al_2O_3$ ratio of 0·7, which is the characteristic value for the most primitive SMIs. The calculated composition of the most primitive melt preserved in the SMIs is given in Table 10 and Fig. 8. As SMIs are absent from the cores of the large olivine grains, it is likely that the most primitive melt represented by the SMIs had already undergone some olivine and potentially clinopyroxene fractionation. This agrees well with the fact that this melt composition is relatively high in $Al_2O_3$ and low in MgO compared with most experimental melts produced by partial melting of garnet lherzolite (Table 10). Crystallization of a significant amount of clinopyroxene before entrapment of the most primitive SMIs is unlikely, as melting of clinopyroxene in the SMIs terminates before remelting of an adequate quantity of olivine from the inclusion walls. Addition of 15 wt % olivine increases the mg-number of the melt to 74, a value expected of a primitive mantle melt in equilibrium with olivine having a mg-number of 91 at 3 GPa using the Fe–Mg exchange coefficient ($Kd = 0{\cdot}36$ at 3 GPa) of Ulmer (1989). Before the addition of olivine we calculated the characteristic $Fe_2O_3/FeO$ ratio of the melt using the equation of Kress & Carmichael (1991) and used only the FeO content for the mg-number calculation. The resulting primitive parental melt is basanitic (43·6 wt % $SiO_2$, mg-number 74) with relatively low total alkali concentrations (4·91 wt % $Na_2O + K_2O$) (Table 10). Similar results can be achieved by adding both olivine and clinopyroxene; however, in this case the CaO concentration becomes too high, whereas the MgO content remains too low compared with the experimental melts of Walter (1998).

Measurement of the water content of the parent melt is not possible because of the slow crystallization, long residence time at high temperatures and reheating during transportation to the surface, which could have allowed significant H loss from the SMIs by diffusion through the host mineral (Danyushevsky *et al.*, 2002). However, crystallization of amphibole in the SMIs and as a cumulate

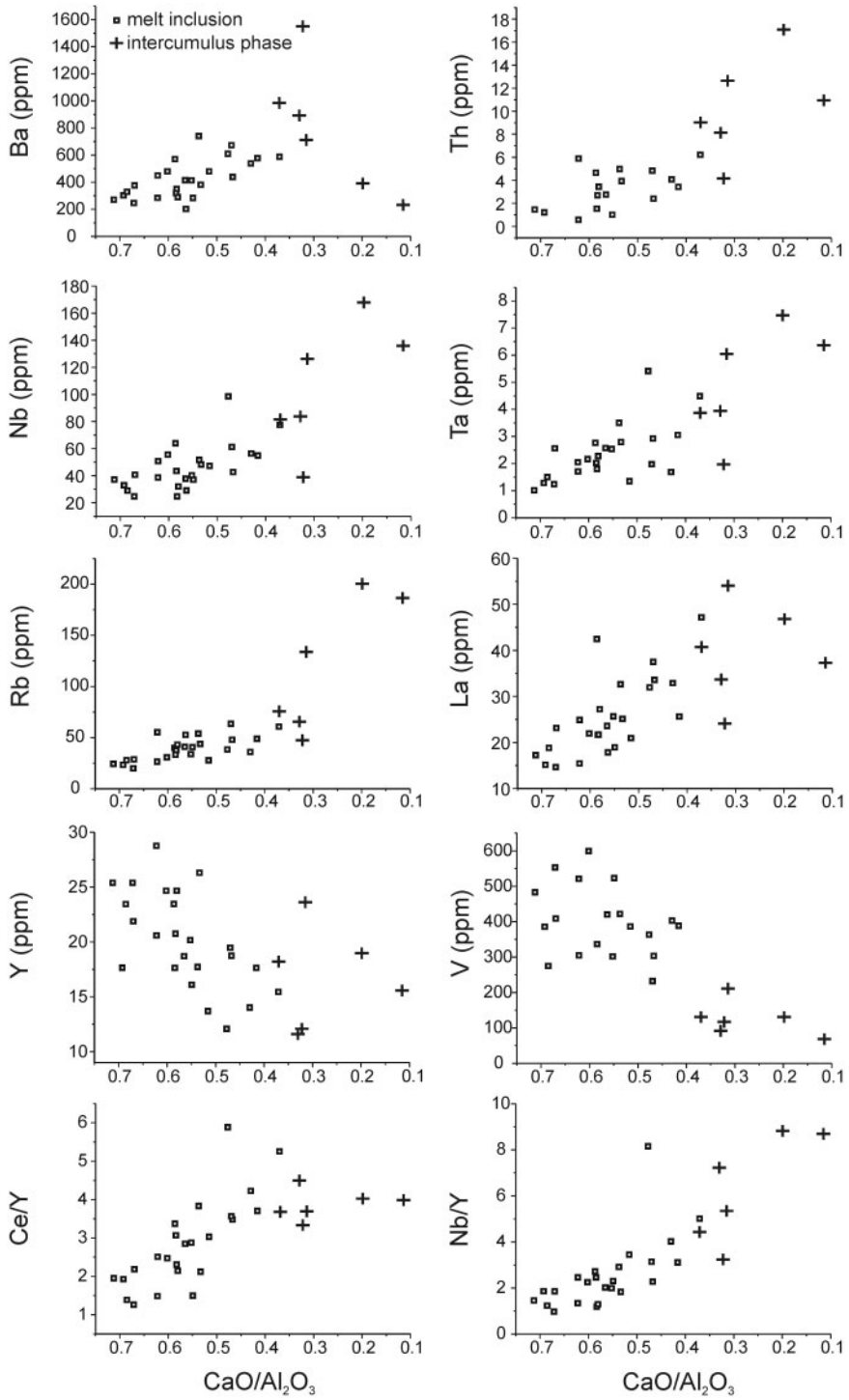


**Fig. 7.** Trace element variation diagrams for the olivine-hosted SMIs as a function of the $CaO/Al_2O_3$ ratio. The bulk composition of the analyzed intercumulus phases is also shown (+), forming continuous trends towards low $CaO/Al_2O_3$ ratios.

xenolith-forming phase indicates that a significant amount of water was present in the melt. Compatibility of $H_2O$ during mantle melting is similar to that of P, Ce and Nd (Aubaud *et al.*, 2004; Bolfan-Casanova, 2005), which would allow us to calculate the $H_2O$ content of the melt if the $H_2O$ content of the mantle source was known. However, there are limited data available on the water content of the subcontinental asthenosphere. Embey-Isztin *et al.* (1993) and Dobosi *et al.* (1995) have shown that Plio-Pleistocene alkaline basalts of the Pannonian–Carpathian

region are derived from an ocean-island basalt (OIB)-like asthenospheric mantle source. Michael (1988) pointed out that $H_2O/(Ce+Nd)$ ratios for mid-ocean ridge basalt (MORB) and OIB vary in a narrow range of $95 \pm 30$. For OIB from Loihi this ratio varies between 107 and 125 (Michael, 1988). Simons *et al.* (2002) drew similar conclusions, suggesting a typical $H_2O/Ce$ ratio of $210 \pm 20$ for a mantle plume and $150 \pm 10$ for a depleted MORB mantle (DMM) component. Minor variations in the above-mentioned elemental ratios between contrasting mantle sources allow their use to estimate the water content of the parental melt of the cumulates assuming an OIB-like mantle plume component as the source. The estimated water content is between 0·73 and 0·85 wt % based on the $H_2O/(Ce+Nd)$ ratios of Michael (1988) and between 0·74 and 0·9 wt % using $H_2O/Ce$ ratios of Simons *et al.* (2002).

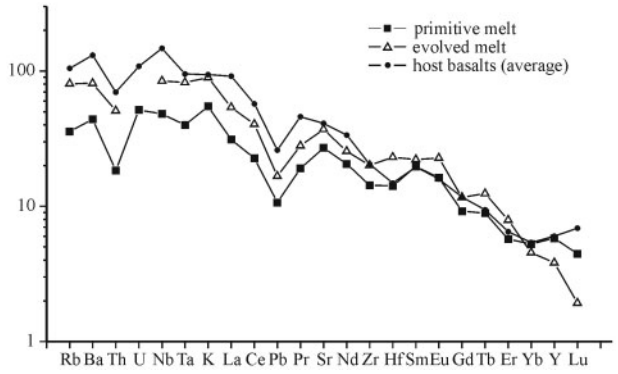


**Fig. 8.** Primitive mantle normalized trace element composition of the primitive and the evolved end of the melt compositions shown by the SMIs. For comparison the average composition of the xenolith-hosting alkaline basalts of the region is also shown (Dobosi and Jenner, 1999).

The presence of $CO_2$ fluid inclusions and heterogeneous entrapment of silicate melt and $CO_2$ in clinopyroxenes (Fig. 3d) indicates $CO_2$ saturation during crystallization. Considering that primary $CO_2$ inclusions are present in crystal cores, $CO_2$ saturation must have occurred close to the temperature of clinopyroxene saturation. The presence of a large amount of heterogeneously entrapped $CO_2$ fluid–silicate melt inclusions in clinopyroxene and lack of $CO_2$ fluid inclusions in olivine indicates that nucleation of the exsolving $CO_2$ happened on the surface of the crystallizing clinopyroxene. According to the volatile saturation model of Dixon (1997) for alkali basalts with 0·8 wt % water, a $CO_2/H_2O$ ratio of approximately three is required to reach volatile saturation at the estimated crystallization pressure of the cumulates. This implies $CO_2$ contents between 2·20 and 2·55 wt % for the parental melt.

## Source of the parental melt

Conditions of parental melt formation can be estimated based on the composition of the SMIs. We modelled the trace element composition of partial melts of a garnet lherzolite and a spinel lherzolite produced by variable degree of partial melting. We selected Nb, Y, Zr and Nd for the

*Table 10: Composition estimations for the parental melt of the cumulate xenoliths*

| | Primitive end of SMI trend | $Fe_2O_3/FeO$ calculated | 15 wt % ol added | 20 wt % ol added | 10 wt % ol and 10 wt % cpx added | Experimental melts of Walter (1998) | |
|---|---|---|---|---|---|---|---|
| | | | | | | 3 GPa, 14% melting | 4 GPa, 9% melting |
| $SiO_2$ | 44·4 | 44·4 | 43·6 | 43·3 | 44·3 | 46·17 | 46·38 |
| $TiO_2$ | 2·36 | 2·36 | 2·02 | 1·90 | 2·04 | 0·91 | 1·45 |
| $Al_2O_3$ | 17·2 | 17·2 | 14·6 | 13·7 | 14·3 | 13·32 | 9·81 |
| FeO | 8·94 | 7·25 | 8·17 | 8·20 | 9·19 | 9·55 | 10·65 |
| $Fe_2O_3$ | | 1·88 | 1·91 | 2·24 | | | |
| MnO | 0·13 | 0·13 | 0·13 | 0·14 | 0·13 | 0·18 | 0·20 |
| MgO | 6·98 | 6·98 | 12·80 | 14·73 | 11·67 | 16·90 | 18·58 |
| CaO | 12·5 | 12·5 | 10·7 | 10·1 | 12·3 | 10·69 | 10·31 |
| $Na_2O$ | 3·47 | 3·47 | 2·95 | 2·78 | 2·83 | 0·96 | 0·93 |
| $K_2O$ | 2·31 | 2·31 | 1·96 | 1·85 | 1·85 | 0·56 | 0·83 |
| $P_2O_5$ | 0·22 | 0·22 | 0·19 | 0·19 | 0·18 | | |
| Total | 98·46 | 98·65 | 99·02 | 99·18 | 98·83 | | |
| mg-no. | 58·2 | 63·2 | 73·6 | 76·2 | 74·3 | 75·9 | 75·7 |
| $CaO/Al_2O_3$ | 0·73 | 0·73 | 0·73 | 0·73 | 0·86 | 0·80 | 1·05 |

Model compositions are calculated by addition of various amounts of olivine (ol) and clinopyroxene (cpx) to the composition of the the most primitive silicate melt inclusions (data in wt %).

model because the analytical uncertainty for these elements is relatively small in the SMI measurements (Table 9). Furthermore, these elements are thought to be insensitive to any potential fluid metasomatism in the source. The asthenospheric upper mantle is inferred to be fertile (i.e. not DMM), based on the isotopic composition of the alkali basalts of the region (Embey-Isztin *et al.*, 1993; Dobosi *et al.*, 1995; Szabó *et al.*, unpublished data). We used the primitive mantle composition of McDonough & Sun (1995) to represent the bulk composition of the source and an internally consistent mineral–melt trace element partitioning dataset from garnet lherzolite melting experiments at pressures between 2·8 and 3·2 GPa (Salters *et al.*, 2002) to model the trace element concentrations in the partial melts. We assumed equilibrium partial melting. Other parameters and results of the model are shown in Fig. 9. Yttrium is compatible in garnet and slightly incompatible in clinopyroxene; consequently, the Y content of the melt is a good indicator of the presence of garnet in the source, but is less affected by the degree of partial melting. Niobium is highly incompatible in all the source minerals, thus it is a good indicator of the degree of partial melting; however, it is not sensitive to the phase proportions in the source. We plotted the calculated primitive parent melt composition on a Nb vs Y diagram (Fig. 9). This shows the degree of partial melting and the garnet/clinopyroxene ratio in the source. To eliminate the uncertainty on the absolute concentrations caused by olivine crystallization before SMI entrapment, we plotted the Nb/Y ratio as a function of the Nd/Zr ratio. As a consequence of the high incompatibility of these elements in olivine, its crystallization does not influence their ratios in the residual melt.

The model indicates partial melting of a garnet lherzolite source with a clinopyroxene/garnet ratio between three and seven. The estimated degree of partial melting is ~2%.

We compared the major element composition of the melt with the experimental data of Walter (1998) for melting of garnet peridotite. The major element concentrations in the parental melt best resemble experimental melts produced by garnet lherzolite melting close to 3 GPa (Table 10). Melting at higher pressures would result in higher MgO and FeO, but significantly lower $Al_2O_3$ and slightly lower CaO concentrations because of the increasing proportion of olivine in the melting mode at the expense of clinopyroxene and garnet. The MgO content is still slightly lower and $Al_2O_3$ content slightly higher in our modelled parental melt composition than in the experimental melt produced at 3 GPa. This might indicate that formation of the melt occurred at even lower pressures, but still in the garnet stability field. The lowest melt fractions produced by Walter (1998) are around 10%, which is a much higher degree of partial melting than that proposed here. This explains the significantly lower incompatible major element (K, Na, Ti) concentrations in the experimental melts, but does not affect significantly the concentrations of $Al_2O_3$, FeO, and MgO, which are buffered by the equilibrium mineral assemblage.

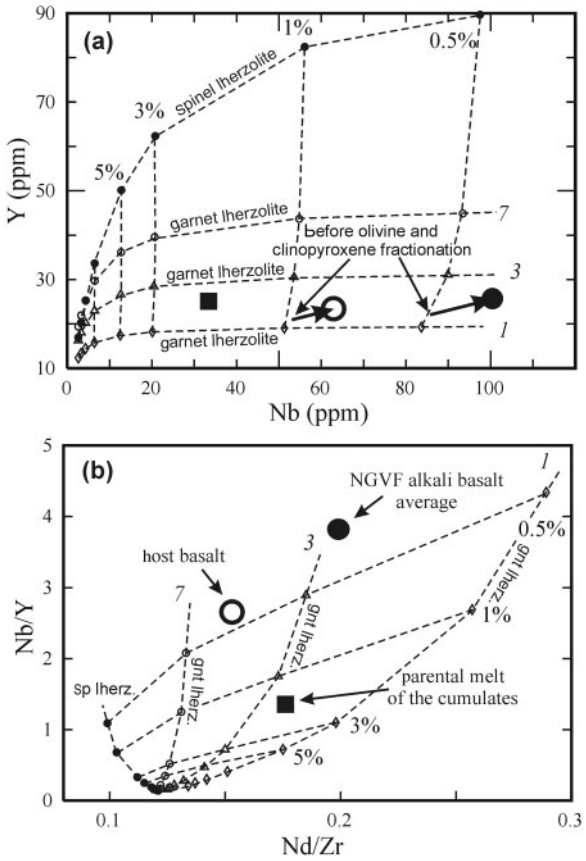


**Fig. 9.** Petrogenetic model calculations. Modelled compositions of partial melts of hypothetical spinel and garnet lherzolites characterized by primitive mantle compositions are shown as a function of the degree of partial melting and the clinopyroxene/garnet ratio in the source. Values in per cent show the degree of partial melting; italic numbers indicate the clinopyroxene/garnet ratio in the hypothetical source. The compositions of the parental melt of the cumulates and the host alkali basalts are also plotted to allow comparison with the modelled partial melt compositions. Arrows in the Nb vs Y diagram (a) show the primitive composition of the host basalt.

## Evolution of the melt

Based on the textural observations (Fig. 2a) and the heating experiments on the SMIs, the first phase to appear on the liquidus is olivine, shortly followed by cotectic crystallization of clinopyroxene. The first melt inclusion entrapment may have occurred when ~15% of the parental magma had crystallized, as 15% olivine fractionation is required to produce the composition of the most primitive melt inclusions from a primitive mantle melt (Table 10). At this stage, olivine was still the dominant phase in the crystallizing mineral assemblage. Subsequently, cotectic equilibrium crystallization of clinopyroxene and olivine

dominated the melt evolution until a late stage when clinopyroxene started to react with the residual liquid to form the characteristic $TiO_2$-rich rims and olivine started to be resorbed (Fig. 2b and c). The clinopyroxene/olivine ratio during crystallization along the olivine–clinopyroxene cotectic must have been high, as the modal proportion of olivine ranges from 20 to 40 vol. % and 15 vol. % olivine must have been crystallized before the onset of clinopyroxene crystallization. Because the most evolved SMIs in olivine have a $CaO/Al_2O_3$ ratio of 0·3 and are approximately two times enriched in the most incompatible trace elements (Nb, Ta, Rb, Ba) (Fig. 7), we suggest that olivine began to react with the residual melt only after ~60 vol. % of the melt had crystallized. Amphibole is an interstitial phase in the xenoliths (Fig. 2f); therefore, its saturation must have happened at a late stage of the melt evolution. In the final stages of crystallization, alkali feldspar, Ti-rich clinopyroxene, apatite and titanomagnetite crystallized from the residual melt (Fig. 2e), leading to an extremely alkaline and $Al_2O_3$-rich residual melt. The presence of compositionally homogeneous glass in the intercumulus phase (Fig. 2d and Table 6) suggests that either there was some melt still present at the time of sampling by the host alkali basalt or the xenoliths were partially melted by the host basalts.

We modelled the evolution of the estimated primitive parental melt using the pMELTS algorithm of Ghiorso *et al.* (2002), assuming equilibrium crystallization at 1 GPa and a value of 0·8 wt % for the initial water content. According to the model olivine appears on the liquidus at 1335°C, and clinopyroxene saturation occurs at 1280°C. Spinel appears at 1220°C. The interval between 1280°C and 1040°C is dominated by clinopyroxene crystallization, simultaneous with precipitation of a minor amount of olivine. At 1040°C Ti-rich clinopyroxene starts to crystallize, followed by amphibole at 1020°C. During amphibole and Ti-rich clinopyroxene crystallization, the amount of olivine decreases slightly and the amounts of normal Ti-poor clinopyroxene and spinel decrease significantly via reaction with the residual melt (Fig. 10). The pMELTS model predicts biotite saturation before the appearance of amphibole; however, biotite was not found in the xenoliths. Thus, we excluded it from the modelled stable phase assemblage. Phase compositions predicted by pMELTS for clinopyroxene have a jadeite component higher than the clinopyroxene cores in the cumulates (Table 11). The low-temperature clinopyroxene has a much higher Ti content than the Ti-rich reaction rims of cumulate clinopyroxene. Assuming equilibrium crystallization, both modelled olivine and clinopyroxene have a lower mg-number close to the solidus than those in the cumulate xenoliths. Furthermore, the clinopyroxene/olivine ratio seems to be slightly overestimated in the crystallizing phase assemblage along the clinopyroxene–olivine cotectic. The high mg-number of olivine and clinopyroxene suggests that they were not in equilibrium with the residual melt throughout the crystallization sequence, but might have been spatially separated from the main body of the residual liquid at some stage. This and potential errors in the model may explain the other discrepancies. The modelled residual melt at 80 vol. % crystallization (reached at 980°C) is characterized by extremely high $Al_2O_3$ (21·4 wt %) and total alkali oxide (16·3 wt %) and high $SiO_2$ (54·7 wt %) similar to the bulk composition of the intercumulus phase assemblage, but is depleted in CaO, MgO and FeO to an even greater extent (Table 11). Therefore, it represents the separated residual melt, except for compatible elements, which could have been buffered by the surrounding peridotite in the main residual melt body. Re-equilibration of the residual melt with peridotite could also be a possible reason for the higher mg-number of the ferromagnesian phases than the values predicted by closed-system crystallization modelling. Below 980°C the program fails to calculate equilibrium. We conclude that the major trends of melt evolution provided by pMELTS, assuming equilibrium crystallization, are generally in good agreement with the textural–mineralogical observations; however, clinopyroxene seems to be slightly overstabilized and there are significant differences in the predicted mineral chemistry. Although the model reproduces the major characteristics of the analytically determined evolutionary trends in melt chemistry, our model assumptions of a closed system and complete equilibrium, and imperfections of the thermodynamic model, may result in significant uncertainties in the numerical values.

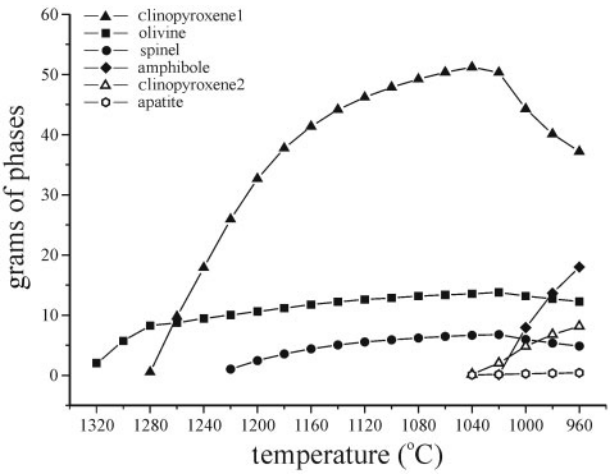


**Fig. 10.** Results of modelling with pMELTS showing the quantity of the minerals crystallized from 100 g of initial melt as a function of temperature (clinopyroxene1, Ti-poor cores; clinopyroxene2, Ti-rich reaction rims).

*Table 11: Phase compositions at 1020°C obtained from pMelts modelling*

| | olivine | clino-pyroxene1 | clino-pyroxene2 | spinel | amphibole | apatite | residual melt |
|---|---|---|---|---|---|---|---|
| $SiO_2$ | 38·1 | 47·2 | 35·2 | | 42·0 | | 51·9 |
| $TiO_2$ | | 2·84 | 11·8 | 1·08 | — | | 1·05 |
| $Al_2O_3$ | | 9·4 | 15·3 | 56·8 | 17·8 | | 21·4 |
| FeO | 24·4 | 5·42 | 4·44 | 16·1 | 6·05 | | 3·39 |
| $Fe_2O_3$ | | 2·25 | 2·08 | 9·17 | 0·02 | | 0·42 |
| MgO | 37·4 | 11·8 | 8·8 | 16·8 | 15·4 | | 1·40 |
| CaO | 0·13 | 19·3 | 21·1 | | 13·1 | 55·8 | 1·70 |
| $Na_2O$ | | 1·68 | 1·22 | | 3·61 | | 7·79 |
| $K_2O$ | | | | | | | 7·37 |
| $P_2O_5$ | | | | | | 42·4 | 0·55 |
| $H_2O$ | | | | | | 1·79 | 2·98 |
| mg-no. | 73·2 | 79·5 | 77·9 | | 81·9 | | 42·4 |

## Garnet precipitation from the parental melt?

Depletion in Y and HREE displayed by both the evolutionary trends in the melt inclusions (Fig. 7) and the trace element zonation in the clinopyroxene (Fig. 4) suggests crystallization of a mineral phase in which these elements are compatible. The most obvious explanation would be the primary magmatic crystallization of garnet. Experimental studies in alkaline basaltic melts, however, have reported stability of garnet only at pressures higher than the estimated pressure conditions at which these cumulates were formed (Green & Ringwood, 1964; Green, 1969, 1973). Amphibole could be a potential host for middle REE (MREE) and HREE, yet most reported partition coefficients in the literature are below one even for these elements (Downes *et al.*, 2004). Furthermore, amphibole appears only at a late stage of crystallization and does not display elevated HREE and Y contents (Fig. 2f and Table 5). Liu *et al.* (2005) reported the presence of garnet-pyroxenite veins from the lithospheric mantle of the North China craton. They interpreted the garnet-pyroxenites to have formed through reaction of an incompatible element-rich silicic melt and mantle lherzolite. A similar scenario appears plausible in the present case, although relicts of garnet-bearing reaction products were not sampled by the host alkaline basalts or have not been found yet. Decreasing HREE and Y content could potentially also be explained by the interaction with garnet-bearing lower crustal granulites, the former (probably pre-Middle-Miocene) presence of which has been reported by Kovács & Szabó (2005) from the same volcanic field. However, Hermann *et al.* (2001) did not observe depletion of HREE and Y in basaltic melts intruded into lower crustal granulites. Furthermore, geobarometric calculations and the absence of plagioclase in the mineral assemblage of the clinopyroxenites indicate higher pressures than those characteristic for the lowermost crust of the study region during and after basin extension in Middle Miocene–Pliocene (~0·8–0·9 GPa) (Horvath, 1993).

## The fate of the residual melt

A major question concerns the fate of the residual melt left behind after cumulate formation. The most likely possibilities are consumption by reaction with the surrounding rocks, *in situ* crystallization, or migration to higher levels of the lithosphere. These will now be considered in turn.

### *Interaction between host rock and evolved alkaline melts as metasomatic agent*

$SiO_2$-undersaturated alkaline mafic magmas intruded into shallow levels of the upper mantle close to the Moho are not in equilibrium with their spinel peridotite host rock. Experimental studies have shown that melts rich in alkalis tend to have high $SiO_2$ contents as a result of the decreasing activity coefficient of silica in the melt at buffered (opx–ol assemblage) silica activity (Baker *et al.*, 1995; Hirschmann *et al.*, 1998). Thus, the first reaction to take place is the consumption of some orthopyroxene in the mantle peridotite. A similar metasomatic interaction between peridotite and basanitic melt, involving dissolution of orthopyroxene simultaneous with clinopyroxene and olivine crystallization, has been described by Shaw (1999) and Shaw *et al.* (2005). This reaction is probably most intense during the early stages of interaction, resulting in an increasing $SiO_2$ content in the residual melt of the cumulates, regardless of the crystallizing mineral assemblage (i.e. clinopyroxene/olivine ratio). Rapid Fe–Mg exchange between mantle olivine and the melt (Gaetani & Watson, 2002; Shaw, 2004) might partially buffer the MgO/FeO ratio in the residual melt, concurrently generating less magnesian olivine in the mantle peridotite. The extent of melt–mantle peridotite interaction depends on the unknown spatial dimensions of the intruded melt bodies (surface/volume ratio); however, enrichment of $SiO_2$ in the early stage of melt evolution appears somewhat faster than expected from closed-system equilibrium crystallization modelling, and the mg-number of the ferromagnesian phases is slightly higher than expected (Fig. 6, Table 11). As shown above, with an increasing degree of crystallization, an extremely alkaline and $Al_2O_3$-rich, but CaO-, MgO- and FeO-poor melt is generated as a result of the absence of plagioclase in the mineral assemblage. As a consequence of early volatile saturation, the $H_2O/CO_2$ ratio and the total amount of volatiles dissolved in the melt also increased. These late-stage residual melts probably migrate through the host peridotite and may be effective metasomatic agents,

probably forming amphiboles and potentially alkali feldspar. Amphibole-bearing lherzolite xenoliths are commonly found in alkali basalts and were also found within the NGVF region (Szabó & Taylor, 1994; Szabó *et al.*, 1996; Kovács *et al.*, 2004). Amphiboles in peridotite xenoliths from Fil'akovo (NFL) show the same trace element pattern as amphiboles in the cumulate xenoliths (Fig. 5). Thus, metasomatism of the source of the peridotite xenolith is likely to be caused by a residual melt of a crystallizing basanitic melt body similar to that considered here. This suggests that amphibole can crystallize directly from the parental melt of the cumulates during its late-stage crystallization, at the expense of previously crystallized clinopyroxene (autometasomatism), and also that late-stage residual melts of underplated mafic alkaline magmas can act as amphibole-forming metasomatic agents in the uppermost lithospheric mantle.

### In situ *crystallization*

Unless the uppermost mantle melt bodies had very large surface/volume ratios, it is unlikely that all the residual melt would have been consumed by metasomatic reactions. Thus, we suggest that at least a part of the residual melt crystallized *in situ*.

Rare lower crustal anorthoclasite and syenite xenoliths have been found together with plagioclase-bearing mafic xenoliths by Huraiova *et al.* (1996) and Kovács *et al.* (2003) in the NGVF. These could represent the residual melt of the cumulates, which migrated to higher lithospheric levels, based on their similar bulk composition. However, in most ultramafic xenolith-bearing basalts in the NGVF, these type of xenoliths are absent (Kovács *et al.*, 2004). Amphibole megacrysts are characteristic constituents of the alkali basalts of the region and have been interpreted as high-pressure crystallization products of the host basalts or as melts of similar composition (Dobosi & Jenner, 1999). Direct crystallization from the host basalt seems unlikely because it should already have crystallized to a much higher degree in the temperature range of amphibole stability than apparent at the time of eruption. The common breakdown of the amphibole megacrysts also indicates that they were in disequilibrium with their host alkali basalts. More probably the megacrysts represent a late-stage crystallization product of an underplated alkali basaltic melt body, potentially the same as that from which the ultramafic cumulates were derived as demonstrated above. This is supported by the similar primitive mantle-normalized trace element patterns of these megacrysts and the amphiboles within the ultramafic cumulate xenoliths (Fig. 5). Potassium feldspar megacrysts are also known from two locations and have been interpreted as crustal fragments (Dobosi & Jenner, 1999). However, from our point of view these could also be late-stage crystallization products of the underplated basanites. This is also supported by the similar high Na/K ratio in the sanidine megacrysts described by Kovács *et al.* (2003) and in the sanidine analyzed in the intercumulus phase (Table 6). In the late stages of melt evolution with progressive degassing, the $H_2O/CO_2$ ratio in the exsolving fluid could have reached high enough values to produce pegmatite-like rocks, which may be the source of the above-mentioned megacrysts.

Kaersutite and sanidine megacrysts found in the Newer Basalts (SE Australia) and in alkali basalts from Scotland have also been interpreted to represent near-solidus crystallization products of alkaline melts introduced into the lithospheric mantle near the Moho (Irving, 1974; Stuckless & Irving, 1976; Aspen *et al.*, 1990). Similarly, Downes *et al.* (2004) suggested that disruption of hornblendite xenoliths crystallized at significant lithospheric depth might be the source of amphibole megacrysts in alkaline basalts.

### *Comparison with the host basalt*

The bulk major element and trace element composition of the host basalt is shown in Table 12. Low Ni and Cr contents compared with the primitive mantle melt values of Frey *et al.* (2000) indicate preliminary olivine fractionation from the melt. Using a Rayleigh-type fractionation model, supposing 300 ppm Ni in the primitive melt and $D^{ol/melt} = 10$ (Nabelek, 1980), 12% olivine fractionation is required to reduce the Ni content to 90 ppm, characteristic of the host basalt (Table 12). Fractionation of significant amounts of clinopyroxene is unlikely because the Sc content (20 ppm) is only slightly lower than the characteristic range for primitive continental alkaline basalts (21–27 ppm) (Wilson & Downes, 1991; Frey *et al.*, 2000). However, the CaO content and $CaO/Al_2O_3$ ratio of the host basalt are too low compared with the experimental melts of Walter (1998), probably because of fractionation of minor amounts of clinopyroxene. We estimated the primitive basalt composition by adding 12 wt % olivine and 7 wt % clinopyroxene to the bulk-rock composition (Table 12). This results in an mg-number, $CaO/Al_2O_3$ ratio and Cr, Sc and Ni contents characteristic of primitive mantle melts. Also, we compared the recalculated compositions with the parent melt of the cumulate xenoliths and the experimental melts of Walter (1998). Our results show slightly lower CaO, FeO, and MgO, and slightly higher $Al_2O_3$ and $SiO_2$ content than the low-degree experimental melts of garnet lherzolite (Table 12). They display the same differences compared with the parental melts of the cumulates, except for the $Al_2O_3$ content, which is almost the same.

The host basanite to the xenoliths contains much higher abundances of incompatible trace elements than the parent melt of the cumulates even after the addition of olivine. Using the same elements to model partial melting, both the absolute trace element concentrations and the trace element ratios indicate that the basanite was formed by a

*Table 12: Estimated primitive composition of the host basanite*

| | Host basalt | 12% olivine + 7% clinopyroxene added | Before assimilation |
|---|---|---|---|
| $SiO_2$ | 47·9 | 46·8 | 45·3 |
| $TiO_2$ | 2·10 | 1·82 | 1·96 |
| $Al_2O_3$ | 16·18 | 13·72 | 11·59 |
| FeO | 8·95 | 9·45 | 11·01 |
| MnO | 0·16 | 0·15 | 0·18 |
| MgO | 6·89 | 11·98 | 14·34 |
| CaO | 9·36 | 9·13 | 9·88 |
| $Na_2O$ | 4·30 | 3·54 | 2·81 |
| $K_2O$ | 2·15 | 1·74 | 0·91 |
| $P_2O_5$ | 0·55 | 0·45 | 0·46 |
| Total | 98·49 | 98·83 | 98·44 |
| mg-no.* | 63·2 | 73·8 | 74·4 |
| $CaO/Al_2O_3$ | 0·58 | 0·67 | 0·85 |
| Sc | 20 | 23 | 27 |
| V | 170 | 157 | 164 |
| Cr | 122 | 314 | 381 |
| Ni | 90 | 241 | 283 |
| Cu | 36 | 30 | 9 |
| Rb | 63 | 51 | 34 |
| Sr | 715 | 585 | 592 |
| Y | 23 | 20 | 20 |
| Zr | 224 | 184 | 174 |
| Nb | 62 | 50 | 36 |
| Ba | 790 | 640 | 601 |
| Cs | 1·0 | 0·8 | 0·7 |
| La | 39 | 32 | 30 |
| Ce | 72 | 59 | 58 |
| Nd | 34 | 28 | 30 |
| Sm | 6·6 | 5·6 | 5·9 |
| Eu | 2·2 | 1·8 | 2·0 |
| Yb | 2·3 | 1·9 | 2·0 |
| Lu | 0·3 | 0·2 | 0·2 |
| Hf | 4·2 | 3·6 | 3·4 |
| Ta | 3·5 | 2·8 | 2·3 |
| Pb | 4·0 | 3·2 | 3·0 |
| Th | 5·5 | 4·5 | 3·0 |
| U | 2·2 | 1·8 | 1·3 |
| Tb | 0·8 | 0·7 | 0·7 |

Major elements in wt %; trace elements in ppm. Modelled composition before assimilation is obtained by subtracting 20 wt % of the intercumulus phase of the cumulates using its average composition.
*Calculated assuming that: $Fe^{2+}/(Fe^{2+}+Fe^{3+}) = 0·8$.

considerably lower degree (~0·5%) of partial melting of a garnet-lherzolite source (Fig. 9).

## Implications for the genesis of alkali basalts

If the parental melt of the cumulates and the host basanite is related to the same melting event in the upper mantle (a very likely scenario for the xenoliths investigated in this study), the batch of melt that reached the surface might have not only incorporated xenoliths and megacrysts but also mixed with the still existing residual melt of a previous magma input into an underplated magma chamber. The presence of a residual melt phase requires a very close temporal relationship between magma pulses, which is uncertain. However, partial assimilation of the low-temperature phases, including alkali feldspar and amphibole crystals and potentially some late-stage residual melt, would result in an enrichment in $Al_2O_3$ and $SiO_2$ but depletion in CaO, MgO and FeO in the contaminated basanitic magma. This would not significantly modify the isotopic signatures, however, because the parental melt of the cumulates probably had the same or a similar asthenospheric source. This process might provide an explanation for the discrepancy between the composition of the experimental melts produced by low-degree partial melting of garnet peridotite (Table 10) and the typical composition of the host basanite (Table 12). For this comparison, we used the recalculated primitive composition of the host alkali basalt. If we assume that an original basanitic melt and the residual melt of the cumulates were mixed in an 8:2 proportion and then recalculate the composition of the mixed melt, we obtain a major element composition that more closely resembles the experimental data of Walter (1998) (Tables 10 and 12). The effect of such a mixing process on the trace element pattern is more difficult to predict, but appears not to be significant as the abundances of most incompatible trace elements in the evolved residual melt of the cumulates closely resemble those in the host basalt.

## Geodynamic consequences

The above petrogenetic model suggests that the garnet lherzolite upper mantle, forming the asthenosphere below the NGVF, underwent a multi-stage melting event. In an early stage, a basanitic melt was produced by ~2% melting. This melt did not reach the surface but was intruded close to the Moho in the lithospheric mantle, forming an underplated melt body and/or veins in the uppermost lithospheric mantle. These bodies thermally and probably chemically partially re-equilibrated with the surrounding upper mantle–lowermost crust, reaching a high degree of crystallization and metasomatizing the adjacent mantle lherzolite. Subsequently, a melting event in the asthenosphere formed basanitic melts by a much smaller (0·5–1%) degree of partial melting. These melts reached the surface and formed the alkali basaltic eruptive centres of the region. All alkaline

basalts (*sensu lato*) of the NGVF postdate the second rifting event in the Pannonian Basin during which significant upwelling of the asthenosphere and stretching of the lithospheric mantle occurred (Szabó *et al.*, 1992; Csontos, 1995; Huismans *et al.*, 2001). Therefore, formation of the host basanitic melt is unlikely to be related to decompression melting of upwelling asthenosphere accompanying basin opening in the Middle–Late Miocene. Formation of the underplated melt bodies from which the cumulates crystallized probably also occurred after the main stage of basin extension, preventing the melts from rising through the crust. This is inconcistent with the models of Szabó *et al.* (1992) and Embey-Isztin *et al.* (1993), who interpreted the formation of the Plio-Pleistocene alkaline basalts as the products of decompression melting of the asthenosphere combined with deep fracturing of the lithosphere and rapid ascent of the melts along these fractures. We suggest that ascent of the host basalts could also have been facilitated by their elevated volatile content, which is a plausible consequence of the lower degree of partial melting. The decreasing degree of partial melting might be explained by the decreasing temperature of the asthenospheric dome formed in the Miocene.

### General implications

Our model, based on the mineralogy and chemistry of SMIs and the intercumulus phase assemblage of clinopyroxenite xenoliths, provides direct evidence that olivine-clinopyroxenite xenoliths, amphibole and alkali feldspar megacryts can be formed by open-system equilibrium crystallization of alkali basaltic melts at $P$–$T$ conditions corresponding to the uppermost lithospheric mantle–lower crust. The common occurrence of these types of xenoliths and megacrysts suggests that partial melting of approximately the same asthenospheric source often pre-dates the main xenolith-bearing phase of alkali basalt volcanism worldwide. These early melts reside in the lithospheric mantle close to the Moho and crystallize at least partially before the surface volcanic activity begins. The residual melt left after crystallization of clinopyroxene and olivine is enriched in volatiles, alkalis and $SiO_2$, and is likely to interact with the surrounding mantle peridotite and/or lower crustal rocks as a metasomatic agent, often forming hydrous minerals.

In the study region the parent melt (basanite) of these cumulates was formed by a significantly higher degree of partial melting (2%) than the host basanite, implying that the volume of the melt bodies trapped in the mantle lithosphere could be larger than that of the basalt, which reached the surface. There is currently no evidence that this difference in the degree of partial melting is necessarily present at other xenolith locations; however, the higher volatile content resulting from the smaller degree of melting could be a general reason explaining why only the later-formed melts can reach the surface.

## CONCLUSIONS

Ultramafic cumulate xenoliths hosted in a Pliocene basanite from the Pannonian Basin indicate that the alkali basaltic volcanism was pre-dated by a higher degree partial melting event of approximately the same or a slightly deeper mantle source in the Nógrád–Gömör Volcanic Field. These higher degree melts did not reach the surface but formed melt bodies via underplating in the subcontinental lithospheric mantle near the Moho. The absence of metamorphic features in the cumulate xenoliths and the striking similarity between the trace element characteristics of their parental melt and those of the host basanite suggest that intrusion of the underplated melt bodies only shortly pre-dated the volcanic activity. Evolution of the melt trapped in the Moho underplate was dominated by major clinopyroxene and minor olivine crystallization in the early stage, followed by amphibole crystallization concurrent with partial resorption of the clinopyroxene and olivine. The residual melt became highly enriched in $Al_2O_3$, alkalis and most incompatible trace elements, enriched in $SiO_2$ and strongly depleted in CaO, FeO, and MgO. This melt could potentially form pegmatite-like bodies at high pressures, which could be the source of the amphibole and sanidine megacrysts most commonly found in the younger eruptive centres of the same volcanic field. Preferential remelting of the later, low-temperature mineral assemblage (sanidine, amphibole) may have contaminated the host basanite. The residual melt of the underplated basanitic melts also acted as a metasomatic agent, forming amphibole in the subcontinental lithospheric upper mantle of the region.

## ACKNOWLEDGEMENTS

The authors would like to thank Enikő Bali and Klára Kóthay for their technical advice during the sample preparation and helpful discussions later. We are grateful to Hilary Downes and Cliff J. Shaw for helping to improve the manuscript with their constructive reviews. We also thank Caroline Harris for correcting the English of the manuscript. This research project was supported by the Hungarian National Science Foundation (TO43686 to C.S.). This is publication 32 of the Lithosphere Fluid Research Laboratory at Eötvös University, in collaboration with the Institute of Isotope Geochemistry and Mineral Resources, ETH Zürich and the Research School of Earth Sciences, ANU Canberra.

## REFERENCES

Aspen, P., Upton, B. G. J. & Dickin, A. P. (1990). Anorthoclase, sanidine and associated megacrysts in scottish alkali basalts—high-pressure syenitic debris from upper mantle sources. *European Journal of Mineralogy* **2**, 503–517.

Aubaud, C., Hauri, E. H. & Hirschmann, M. M. (2004). Hydrogen partition coefficients between nominally anhydrous minerals and basaltic melts. *Geophysical Research Letters* **31**, doi:10.1029/2004GL021341.

Baker, M. B., Hirschmann, M. M., Ghiorso, M. S. & Stolper, E. M. (1995). Compositions of near-solidus peridotite melts from experiments and thermodynamic calculations. *Nature* **375**, 308–311.

Ballhaus, C., Berry, R. F. & Green, D. H. (1991). High-pressure experimental calibration of the olivine–orthopyroxene–spinel oxygen geobarometer—implications for the oxidation-state of the upper mantle. *Contributions to Mineralogy and Petrology* **107**, 27–40.

Bertagnini, A., Metrich, N., Landi, P. & Rosi, M. (2003). Stromboli volcano (Aeolian Archipelago, Italy): an open window on the deep-feeding system of a steady state basaltic volcano. *Journal of Geophysical Research-Solid Earth* **108**, (B7), doi:10.1029/2002JB002146.

Bolfan-Casanova, N. (2005). Water in the Earth's mantle. *Mineralogical Magazine* **69**, 229–257.

Bondi, M., Morten, L., Nimis, P., Rossi, P. L. & Tranne, C. A. (2002). Megacrysts and mafic–ultramafic xenolith-bearing ignimbrites from Sirwa Volcano, Morocco: phase petrology and thermobarometry. *Mineralogy and Petrology* **75**, 203–221.

Cervantes, P. & Wallace, P. (2003). Magma degassing and basaltic eruption styles: a case study of similar to 2000 year BP Xitle volcano in central Mexico. *Journal of Volcanology and Geothermal Research* **120**, 249–270.

Chen, S. H., O'Reilly, S. Y., Zhou, X. H., Griffin, W. L., Zhang, G. H., Sun, M., Feng, J. L. & Zhang, M. (2001). Thermal and petrological structure of the lithosphere beneath Hannuoba, Sino-Korean Craton, China: evidence from xenoliths. *Lithos* **56**, 267–301.

Csontos, L. (1995). Tertiary tectonic evolution of the Intra-Carpathian area: a review. *Acta Vulcanologica* **7**, 1–13.

Danyushevsky, L. V., Della-Pasqua, F. N. & Sokolov, S. (2000). Re-equilibration of melt inclusions trapped by magnesian olivine phenocrysts from subduction-related magmas: petrological implications. *Contributions to Mineralogy and Petrology* **138**, 68–83.

Danyushevsky, L. V., McNeill, A. W. & Sobolev, A. V. (2002). Experimental and petrological studies of melt inclusions in phenocrysts from mantle-derived magmas: an overview of techniques, advantages and complications. *Chemical Geology* **183**, 5–24.

Danyushevsky, L. V., Perfit, M. R., Eggins, S. M. & Falloon, T. J. (2003). Crustal origin for coupled 'ultra-depleted' and 'plagioclase' signatures in MORB olivine-hosted melt inclusions: evidence from the Siqueiros Transform Fault, East Pacific Rise. *Contributions to Mineralogy and Petrology* **144**, 619–637.

Dixon, J.E. (1997). Degassing of alkalic basalts. *American Mineralogist* **82**, 368–378 .

Dobosi, G. & Jenner, G. A. (1999). Petrologic implications of trace element variation in clinopyroxene megacrysts from the Nograd volcanic province, north Hungary: a study by laser ablation microprobe-inductively coupled plasma-mass spectrometry. *Lithos* **46**, 731–749.

Dobosi, G., Fodor, R.V. & Goldberg, S. A. (1995). Late-Cenozoic alkalic basalt magmatism in Northern Hungary and Slovakia: petrology, source compositions and relationships to tectonics. *Acta Vulcanologica* **7**, 219–229.

Dobosi, G., Downes, H., Embey-Isztin, A. & Jenner, G. A. (2003). Origin of megacrysts and pyroxenite xenoliths from the Pliocene alkali basalts of the Pannonian Basin (Hungary). *Neues Jahrbuch für Mineralogie, Abhandlungen* **178**, 217–237.

Downes, H., Seghedi, I., Szakács, A., Dobosi, G., James, D. E., Vaselli, O., Rigby, I. J., Ingram, G. A., Rex, D. & Pécskay, Z. (1995). Petrology and geochemistry of Late Tertiary–Quaternary mafic alkaline volcanism in Romania. *Lithos* **35**, 65–81.

Downes, H., Beard, A. & Hinton, R. (2004). Natural experimental charges: an ion-microprobe study of trace element distribution coefficients in glass-rich hornblendite and clinopyroxenite xenoliths. *Lithos* **75**, 1–17.

Embey-Isztin, A. & Dobosi, G. (1995). Mantle source characteristics for Miocene–Pleistocene alkali basalts, Carpathian–Pannonian region: a review of trace elements and isotopic compositions. *Acta Vulcanologica* **7**, 155–166.

Embey-Isztin, A., Scharbert, H. G., Dietrich, H. & Poultidis, H. (1990). Mafic granulites and clinopyroxenite xenoliths from the Transdanubian volcanic region (Hungary)—implications for the deep structure of the Pannonian Basin. *Mineralogical Magazine* **54**, 463–483.

Embey-Isztin, A., Downes, H., James, D. E., Upton, B. G. J., Dobosi, G., Ingram, G. A., Harmon, R. S. & Scharbert, H. G. (1993). The petrogenesis of Pliocene alkaline volcanic rocks from the Pannonian Basin, eastern Central Europe. *Journal of Petrology* **34**, 317–343.

Fodor, L., Csontos, L., Bada, G., Györfi, I. & Benkovics, L. (1999). Tertiary tectonic evolution of the Pannonian basin system and neighboring orogens, a new synthesis of paleostress data. In: Durand, B., Jolivet, L., Horvath, F. & Seranne, M. (eds) *The Mediterranean Basins: Tertiary Extension within the Alpine Orogen. Geological Society, London, Special Publications* **156**, 295–334.

Frey, F. A. & Prinz, M. (1978). Ultramafic inclusions from San Carlos, Arizona—petrologic and geochemical data bearing on their petrogenesis. *Earth and Planetary Science Letters* **38**, 129–176.

Frey, F. A., Clague, D., Mahoney, J. J. & Sinton, J. M. (2000). Volcanism at the edge of the Hawaiian plume: petrogenesis of submarine alkalic lavas from the North Arch volcanic field. *Journal of Petrology* **41**, 667–691.

Gaetani, G. A. & Watson, E. B. (2002). Modeling the major-element evolution of olivine-hosted melt inclusions. *Chemical Geology* **183**, 25–41.

Ghiorso, M. S., Hirschmann, M. M., Reiners, P. W. & Kress, V. C. (2002). The pMELTS: a revision of MELTS for improved calculation of phase relations and major element partitioning related to partial melting of the mantle to 3 GPa. *Geochemistry, Geophysics, Geosystems* **3**, doi:10.1029/2001GC000217.

Green, D. H. (1969). Origin of basaltic and nephelinitic magmas in Earth's mantle. *Tectonophysics* **7**, 409–422.

Green, D. H. (1973). Conditions of melting of basanite magma from garnet peridotite. *Earth and Planetary Science Letters* **17**, 456–465.

Green, D. H. & Ringwood, A. E. (1964). Fractionation of basalt magmas at high pressures. *Nature* **201**, 1276–1279.

Halter, W. E., Pettke, T. Heinrich, C.A. & Rothen-Rutishauser, B. (2002). Major to trace element analysis of melt inclusions by laser-ablatim ICP-MS: methods of quantification. *Chemical Geology* **183**, 63–86.

Hermann, J., Muntener, O. & Gunther, D. (2001). Differentiation of mafic magma in a continental crust-to-mantle transition zone. *Journal of Petrology* **42**, 189–206.

Hirschmann, M. M., Baker, M. B. & Stolper, E. M. (1998). The effect of alkalis on the silica content of mantle-derived melts. *Geochimica et Cosmochimica Acta* **62**, 883–902.

Horváth, F. (1993). Towards a mechanical model for the formation of the Pannonian Basin. *Tectonophysics* **226**, 333–357.

Huismans, R. S., Podladchikov, Y. Y. & Cloetingh, S. (2001). Dynamic modeling of the transition from passive to active rifting, application to the Pannonian basin. *Tectonics* **20**, 1021–1039.

Huraiova, M., Konecny, P., Konecny, V., Simon, K. & Hurai, V. (1996). Mafic and salic igneous xenoliths in late Tertiary

alkaline basalts: fluid inclusion and mineralogical evidence for a deep-crustal magmatic reservoir in the western Carpathians. *European Journal of Mineralogy* **8**, 901–916.

Irving, A. J. (1974). Megacrysts from Newer Basalts and other basaltic rocks of Southeastern Australia. *Geological Society of America Bulletin* **85**, 1503–1514.

Irving, A. J. & Frey, F. A. (1984). Trace-element abundances in megacrysts and their host basalts—constraints on partition coefficients and megacryst genesis. *Geochimica et Cosmochimica Acta* **48**, 1201–1221.

Kamenetsky, V. & Clocchiatti, R. (1996). Primitive magmatism of Mt Etna: insights from mineralogy and melt inclusions. *Earth and Planetary Science Letters* **142**, 553–572.

Kamenetsky, V. S., Crawford, A. J., Eggins, S. & Muhe, R. (1997). Phenocryst and melt inclusion chemistry of near-axis seamounts, Valu Fa Ridge, Lau Basin: insight into mantle wedge melting and the addition of subduction components. *Earth and Planetary Science Letters* **151**, 205–223.

Kovács, I. & Szabó, C. (2005). Petrology and geochemistry of granulite xenoliths beneath the Nograd–Gomor Volcanic Field, Carpathian–Pannonian Region (N Hungary/S Slovakia). *Mineralogy and Petrology* **85**, 269–290.

Kovács, I., Bali, E., Kóthay, K., Szabó, C. & Nédli, Z. (2003). Petrogenetic significance of quartz and feldspar xenocrysts in basaltic rocks. *Földtani Közlöny* **133**, 394–420.

Kovács, I., Zajacz, Z. & Szabó, C. (2004). Type-II xenoliths and related metasomatism from the Nograd–Gomor Volcanic Field, Carpathian–Pannonian region (northern Hungary–southern Slovakia). *Tectonophysics* **393**, 139–161.

Kress, V. C. & Carmichael, I. S. E. (1991). The compressibility of silicate liquids containing $Fe_2O_3$ and the effect of composition, temperature, oxygen fugacity and pressure on their redox states. *Contributions to Mineralogy and Petrology* **108**, 82–92.

Kuzmin, D. V. & Sobolev, A. V. (2004). Boundary layer contribution to the composition of melt inclusions in olivine. *Geochimica et Cosmochimica Acta* **68**, 544.

Liu, Y. S., Gao, S., Lee, C. T. A., Hu, S. H., Liu, X. M. & Yuan, H. L. (2005). Melt–peridotite interactions: links between garnet pyroxenite and high-Mg-number signature of continental crust. *Earth and Planetary Science Letters* **234**, 39–57.

Maclennan, J., McKenzie, D., Hilton, F., Gronvold, K. & Shimizu, N. (2003). Geochemical variability in a single flow from northern Iceland. *Journal of Geophysical Research: Solid Earth* **108**(B1), doi:10.1029/2000JB000142.

McDonough, W. F. & Sun, S. S. (1995). The composition of the Earth. *Chemical Geology* **120**, 223–253.

Michael, P. J. (1988). The concentration, behavior and storage of $H_2O$ in the suboceanic upper mantle—implications for mantle metasomatism. *Geochimica et Cosmochimica Acta* **52**, 555–566.

Nabelek, P. I. (1980). Nickel partitioning between olivine and liquid in natural basalts—Henry's Law behavior. *Earth and Planetary Science Letters* **48**, 293–302.

Nielsen, R. L., Crum, J., Bourgeois, R., Hascall, K., Forsythe, L. M., Fisk, M. R. & Christie, D. M. (1995). Melt inclusions in high-an plagioclase from the Gorda Ridge—an example of the local diversity of MORB parent magmas. *Contributions to Mineralogy and Petrology* **122**, 34–50.

Norman, M. D., Garcia, M. O., Kamenetsky, V. S. & Nielsen, R. L. (2002). Olivine-hosted melt inclusions in Hawaiian picrites: equilibration, melting, and plume source characteristics. *Chemical Geology* **183**, 143–168.

Putirka, K. (1999). Clinopyroxene plus liquid equilibria to 100 kbar and 2450 K. *Contributions to Mineralogy and Petrology* **135**, 151–163.

Putirka, K. D., Mikaelian, H., Ryerson, F. & Shaw, H. (2003). New clinopyroxene–liquid thermobarometers for mafic, evolved, and volatile-bearing lava compositions, with applications to lavas from Tibet and the Snake River Plain, Idaho. *American Mineralogist* **88**, 1542–1554.

Riley, T. R. & Bailey, A. K. (2003). Barium-rich sanidine megacrysts from the West Eifel (Germany). *Neues Jahrbuch für Mineralogie, Monatshefte* **1**, 18–30.

Royden, L., Horvath, F., Nagymarosy, A. & Stegena, L. (1983a). Evolution of the Pannonian Basin system. 2. Subsidence and thermal history. *Tectonics* **2**, 91–137.

Royden, L., Horvath, F. & Rumpler, J. (1983b). Evolution of the Pannonian Basin system. 1. Tectonics. *Tectonics* **2**, 63–90.

Salters, V. J. M., Longhi, J. E. & Bizimis, M. (2002). Near mantle solidus trace element partitioning at pressures up to 3·4 GPa. *Geochemistry, Geophysics, Geosystems* **3**(7), doi:10.1029/2001GC000148.

Schiano, P. (2003). Primitive mantle magmas recorded as silicate melt inclusions in igneous minerals. *Earth-Science Reviews* **63**, 121–144.

Schiano, P., Clocchiatti, R., Ottolini, L. & Sbrana, A. (2004). The relationship between potassic, calc-alkaline and Na-alkaline magmatism in South Italy volcanoes: a melt inclusion approach. *Earth and Planetary Science Letters* **220**, 121–137.

Seghedi, I., Downes, H., Vaselli, O., Szakács, A., Balogh, K. & Pécskay, Z. (2004). Post-collisional Tertiary–Quaternary mafic alkalic magmatism in the Carpathian–Pannonian region: a review. *Tectonophysics* **393**, 43–62.

Shaw, C. S. J. (1999). Dissolution of orthopyroxene in basanitic magma between 0·4 and 2 GPa: further implications for the origin of Si-rich alkaline glass inclusions in mantle xenoliths. *Contributions to Mineralogy and Petrology* **135**, 114–132.

Shaw, C. S. J. (2004). The temporal evolution of three magmatic systems in the West Eifel volcanic field, Germany. *Journal of Volcanology and Geothermal Research* **131**, 213–240.

Shaw, C. S. J. & Eyzaguirre, J. (2000). Origin of megacrysts in the mafic alkaline lavas of the West Eifel volcanic field, Germany. *Lithos* **50**, 75–95.

Shaw, C. S. J., Eyzaguirre, J., Fryer, B. & Gagnon, J. (2005). Regional variations in the mineralogy of metasomatic assemblages in mantle xenoliths from the West Eifel Volcanic Field, Germany. *Journal of Petrology* **46**, 945–972.

Simons, K., Dixon, J., Schilling, J. G., Kingsley, R. & Poreda, R. (2002). Volatiles in basaltic glasses from the Easter–Salas y Gomez Seamount Chain and Easter Microplate: implications for geochemical cycling of volatile elements. *Geochemistry, Geophysics, Geosystems* **3**, doi:10.1029/2001GC000173.

Stuckless, J. S. & Irving, A. J. (1976). Strontium isotope geochemistry of megacrysts and host basalts from Southeastern Australia. *Geochimica et Cosmochimica Acta* **40**, 209–213.

Szabó, C. & Taylor, L. (1994). Mantle petrology and geochemistry beneath Nógrád–Gömör Volcanic Field, Carpathian–Pannonian region. *International Geology Review* **36**, 328–358.

Szabó, C., Harangi, S. & Csontos, L. (1992). Review of Neogene and Quaternary volcanism of the Carpathian–Pannonian region. *Tectonophysics* **208**, 243–256.

Szabó, C., Bodnar, R. J. & Sobolev, A. V. (1996). Metasomatism associated with subduction-related, volatile-rich silicate melt in the upper mantle beneath the Nograd–Gomor volcanic field, northern Hungary–southern Slovakia: evidence from silicate melt inclusions. *European Journal of Mineralogy* **8**, 881–899.

Török, K., Bali, E., Szabo, C. & Szakal, J. A. (2003). Sr-barite droplets associated with sulfide blebs in clinopyroxene megacrysts from basaltic tuff (Szentbekkalla, western Hungary). *Lithos* **66**, 275–289.

Ulmer, P. (1989). The dependence of the $Fe^{2+}$–Mg cation-partitioning between olivine and basaltic liquid on pressure, temperature and composition—an experimental study to 30 kbars. *Contributions to Mineralogy and Petrology* **101**, 261–273.

Walter, M. J. (1998). Melting of garnet peridotite and the origin of komatiite and depleted lithosphere. *Journal of Petrology* **39**, 29–60.

Wilson, M. & Downes, H. (1991). Tertiary–Quaternary extension-related alkaline magmatism in Western and Central Europe. *Journal of Petrology* **32**, 811–849.

Xu, J. H., Chu, X. L., Zhou, Y. M. & Du, Y. F. (1999). Sulfide-melt inclusions in mantle xenoliths of Hannuoba, China. *Chinese Science Bulletin* **44**, 166–170.

Zajacz, Z. & Szabó, C. (2003). Origin of sulfide inclusions in cumulate xenoliths from Nograd–Gomor Volcanic Field, Pannonian Basin (north Hungary/south Slovakia). *Chemical Geology* **194**, 105–117.

# APPENDIX

## Quantification of the SMI compositions

Trace element data were obtained by LA-ICPMS analysis of unheated multiphase SMIs in olivine. For quantification of the LA-ICPMS measurements we used the method of Halter *et al.* (2002), which is based on ablation of entire SMIs along with their host mineral. This approach requires knowledge of the concentration of an element in both the SMI (i.e. internal standard) and its host to calculate the mass ratio between the host mineral and the SMI in the mixed signal. With the mass ratio and the composition of the host mineral, the composition of the SMI can be calculated from the mixed signal. The easiest way to obtain an internal standard is to use homogenized SMI data from the same sample, particularly if the SMIs show only a small compositional variability. In this case, one characteristic element concentration might be used to determine the mass ratio. In the studied cumulate xenoliths, SMIs show a compositional trend that represents the evolution of the parent melt (see above). Therefore, there is no element with a constant concentration that could be used as an internal standard to determine the mass ratio. However, $CaO/Al_2O_3$ and $CaO/(Na_2O+K_2O)$ ratios are the same both in the SMI and in the mixed signal because all these elements are highly incompatible in the host olivine (0·00 wt % for $Al_2O_3$, $Na_2O$, and $K_2O$, and 0·03–0·19 wt % for CaO), thus the only contribution to the signal comes from the SMI. The plot of $CaO/(Na_2O+K_2O)$ as a function of $CaO/Al_2O_3$ shows a steep slope with a nearly linear correlation across a wide range (Fig. A1). This indicates that the LA-ICPMS analyses of the SMIs show the same negative correlation between the $CaO/Al_2O_3$ ratio and the total abundance of alkali elements in the melt as shown by the composition of the homogenized SMIs. This provides a solid basis for use of the total abundance of alkali oxides as an internal standard, because this quantity can be calculated as a function of the $CaO/Al_2O_3$ ratio using the trend shown by the homogenized SMI data. Instead of simply fitting a trend

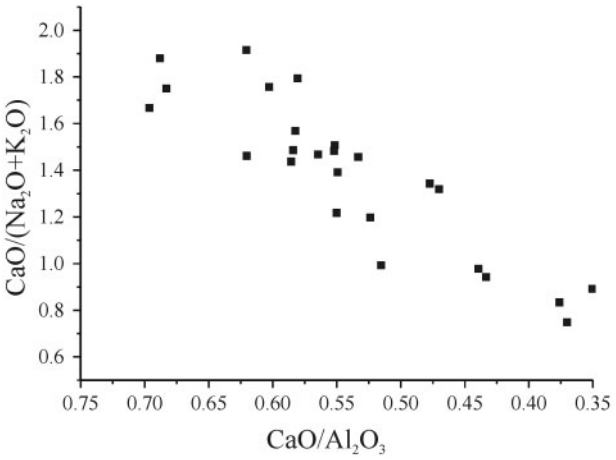


**Fig. A1.** $CaO/(Na_2O+K_2O)$ vs $CaO/Al_2O_3$ shown by the LA-ICPMS analysis data before deconvolution of the host mineral (olivine) and the olivine-hosted melt inclusion signal. It should be noted that the elements used are all incompatible in the host olivine; thus, their ratio is determined only by the composition of the SMIs. The trend shown therefore represents the evolution of the parental melt of the cumulates.

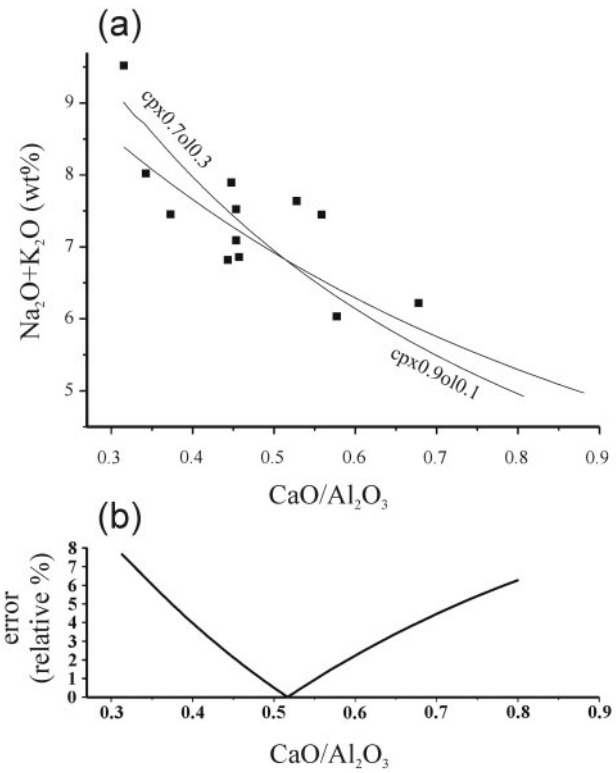


**Fig. A2.** Model to quantify the LA-ICPMS analyses. (a) Symbols show the composition of the homogenized SMIs. These data were fitted with modelled evolutionary trends assuming different ratios of clinopyroxene and olivine in the crystallizing mineral assemblage. The curves indicate cpx0·9ol0·1 (clinopyroxene 90%–olivine 10% relative) and cpx0·7ol0·3 (clinopyroxene 70%–olivine 30% relative) in the crystallizing assemblage. (b) Error resulting from the uncertainty in the assumed clinopyroxene/olivine ratio.

line to the observed homogenized SMI data, we modelled melt evolution assuming constant clinopyroxene/olivine ratios in the crystallizing assemblage [this is indicated by the linearity of $CaO/Al_2O_3$ vs $CaO/(Na_2O + K_2O)$ trend] to define the shape of the trend line used to fit the SMI data (Fig. A2a). The modal composition of the cumulates suggests that the crystallization was dominated by clinopyroxene (Kovács et al., 2004). Consequently, we assumed that the olivine/clinopyroxene ratio in the crystallization mode was in the range of 1/9 to 3/7, as indicated by the modal compositions of the xenoliths (Kovács et al., 2004). Using this fit the total alkali content of the melt can be calculated from the $CaO/Al_2O_3$ ratio, which can be derived from the mixed signal of the olivine-hosted SMIs before the deconvolution of the host mineral and SMIs. The calculated total alkali content then can be used as an internal standard to determine the mass ratio of the host olivine and the SMIs in the mixed signal and to calculate the SMI composition. The model involves some uncertainties because of the ambiguity in the clinopyroxene to olivine ratio during crystallization of the cumulate body. We calculated the possible maximum error resulting from this modelling as a function of the $CaO/Al_2O_3$ ratio of the melt (Fig. A2b). This uncertainty is smaller than the analytical uncertainty for most elements, but is enlarged by the natural variability of the SMIs. Overall, we can conclude that quantification of the chemical composition of the SMIs has $\sim$10% relative uncertainties on the determination of the mass factor. This will result in a high uncertainty for elements that are compatible in the host olivine (namely Mg, Fe, Ni), but only 10% uncertainty for all the other elements that are highly incompatible. Therefore, we used only elements incompatible in olivine for interpretation.